Available online at www.sciencedirect.com
ScienceDirect
Comput. Methods Appl. Mech. Engrg. 196 (2007) 4222–4249
Computer methods in applied mechanics and engineering
www.elsevier.com/locate/cma

A novel boundary element approach to time-harmonic dynamics of incremental nonlinear elasticity: The role of pre-stress on structural vibrations and dynamic shear banding

D. Bigoni [a,*], D. Capuani [b], P. Bonetti [a], S. Colli [a]

[a] *Dipartimento di Ingegneria Meccanica e Strutturale, Università di Trento, Via Mesiano, 77-38050 Povo, Trento, Italy*
[b] *Dipartimento di Architettura, Università di Ferrara, Via Quartieri, 8-44100 Ferrara, Italy*

Received 10 April 2006; received in revised form 18 April 2007; accepted 23 April 2007
Available online 24 May 2007

Abstract

A new boundary element technique is developed to analyze two-dimensional, time-harmonic, small-amplitude vibrations, superimposed upon a homogeneously pre-stressed, orthotropic and incompressible elastic solid. New expressions for the Green's functions for incremental applied tractions are obtained, in which 'static' and 'dynamic' contributions are uncoupled. The dynamic contributions are regular, whereas the static terms are strongly singular and are solved in closed-form expressions, particularly useful for numerical calculations. As a consequence of the static/dynamic de-coupling, these expressions turn out to be useful also for quasi-static deformation. The formulation is tested for different boundary value problems. These include a problem with certain boundary conditions investigated by Ryzhak in the static case, for which an analytic solution is proposed here in the time-harmonic regime. The effect of pre-stress is shown to strongly influence the vibrational response of elastic structures. It is shown that natural frequencies strongly decrease when pre-stress approaches quasi-static bifurcation loads and wave propagation speeds tend to vanish when the boundary of ellipticity is approached. Near this boundary (but still within the elliptic region) we observe a focussing of vibrations along plane waves parallel to the shear bands.

Keywords: Time-harmonic dynamics; Non-linear elasticity; Vibrations

1. Introduction

Pre-stress induced by ribs in soundboards is essential to the correct vibrational performance of stringed musical instruments [4,9]: this is but one among many examples showing that pre-stress strongly influences dynamical properties of structures. Accordingly, effects of pre-stress in time-harmonic dynamics have been extensively analyzed in elasticity (see, among others [7,18,19,38,43] and references quoted therein), for structures [20,41], plates [13,23,36], concrete members, inflatable and tensegrity structures [25,29,47], vibration isolators [27,46], resonant devices in MEMS [39], and geological structures [26].

However, although well developed in linear elasticity (see for instance [3,15,17,32]), a boundary element technique has never been formulated in the dynamic range when pre-stress is included.

* Corresponding author. Tel.: +39 0461 882507; fax: +39 0461 882599.
E-mail addresses: bigoni@ing.unitn.it (D. Bigoni), d.capuani@unife.it (D. Capuani).
URL: http://www.ing.unitn.it/~bigoni/ (D. Bigoni).

0045-7825/$ - see front matter
doi:10.1016/j.cma.2007.04.013

A general boundary element technique for *quasi-static*, two-dimensional and incremental elastic nonlinear deformations has been proposed by Bigoni and Capuani [5] and Brun et al. [11]. In the present paper, the formulation is generalized to *dynamic, time-harmonic* incremental loading, exploiting the Green's function and boundary integral equations recently obtained by Bigoni and Capuani [6]. Those results are complemented here by the derivation of new expressions for the Green's functions for incremental applied tractions, where singular terms only appear in the quasi-static contributions, decoupled from dynamic terms. The singular terms are determined in closed form, providing new expressions which not only yield a simpler and more effective approach to numerical calculations, but prove essential to the treatment of strongly-singular integrals involved in the boundary integral equations.

When applied to homogeneously pre-stressed domains[1], the proposed formulation retains the essential advantage that only the boundary of the body is discretized and no 'artificial' volume terms are introduced, such as for instance those present in the so-called 'dual reciprocity bem' for linear elasticity [24,30,37]. The methodology proposed in this paper shares certain similarities to approaches developed for anisotropic elasticity in the absence of pre-stress [1,2,14,16,21,34,49] although the incompressibility constraint and presence of pre-stress make the formulation essentially different. The issue of isochoric elastic deformation pertains to standard formulations of finite elasticity (in particular we refer to [8]), the framework allowing consideration of the pre-stress effects, when incremental deformations are considered. Under small strain, the incompressibility constraint has been little investigated for time-harmonic dynamics (see [40], which is restricted to isotropic behaviour).

The proposed methodology is shown to evidence capabilities, which, in addition to the advantages known for boundary elements employed under quasi-static loading (discretization of the contour only, insensitivity to incompressibility constraint, and the capability to analyze singularities), includes also the ability to keep radiation damping [22] into account, without the typical expedients of finite elements (where viscous/damping [50], or transmitting [28] boundaries, or infinite elements [35] are introduced; see also [51] and references cited therein).

The formulation developed in the present article allows us to attack problems of time-harmonic vibrations in the presence of pre-stress, revealing its important role. In particular, the pre-stress can be used as a parameter to approach the elliptic boundary[2], at which strain rate discontinuities become possible in the form of shear bands. We can therefore follow the perturbative approach proposed by Bigoni and Capuani [5,6] and analyze shear band emergence in dynamic conditions. In this context, the class of boundary value problems analyzed by Ryzhak [44,45] plays a prominent role, since stability and uniqueness are certain within strong ellipticity for those problems. In particular, we solve the shear deformation of a pre-stressed orthotropic elastic block, with 'sliding along parallel lines' boundary conditions, and we provide an analytical closed-form solution, which turns out to be useful to evaluate the vibrational effects of pre-stress and the numerical performance of the proposed boundary element method. Our results show:

- the significant influence of pre-stress on the vibration natural frequencies, which tend to zero when either a bifurcation load or loss of ellipticity is approached;
- that, consistently with our previous findings (see [5,12] for quasi-static deformation and [6] for time-harmonic dynamics) and still within the elliptic regime, shear bands are revealed with a perturbation technique (evidencing peculiar features, like focussing of vibration into plane waves, parallel to the shear bands that would form at ellipticity loss), even in situations in which they would be excluded by conventional techniques (for instance, the occurrence of shear bands is shown for a Mooney–Rivlin elastic material);
- the different efficiency of the numerical procedures based on two alternative formulations of the traction Green's function. The best formulation leads to a reduction of CPU times up to 90%, together with a sensible increase in precision.

The paper is organized as follows. After a brief presentation of the incremental constitutive equations (see also [8,11]) is given, the Green's function is presented in Section 3 and, additionally to the results given in [6], we provide the gradient of the Green's function for incremental displacements and in-plane hydrostatic stress increment, essential for the boundary element technique. New expressions for Green's functions for incremental applied tractions are derived in Section 4, employing the plane wave expansion formalism (see [6]). These expressions are the key issue for setting the boundary integral technique presented in Section 5. Section 6 is devoted to numerical examples employed to test our formulation and also to highlight the role of pre-stress. In particular, we address: (i) the problem of an elastic hollow cylinder subject to internal time-harmonic pulsating pressure (an example for which the analytical solution is known, thus providing a useful test for our formulation); (ii) a circular hole in an infinite elastic sheet loaded on portions of the boundary (an example evidencing one of the advantages of the present formulation, namely, that radiation damping is automatically taken into account); (iii) a rectangular elastic block, subject to time-harmonic loading distributed on portions of the edges, and with

[1] Inhomogeneity of stress state or elastic properties can however be analyzed by employing a multidomain technique not investigated here for brevity.
[2] Regime classification for time-harmonic dynamics coincides with the classification for quasi-static regime, see [6,42].

different levels of pre-stress (an example revealing the strong effect of pre-stress on the natural vibrations of the system); (iv) a number of examples involving Ryzhak boundary conditions [44,45], one of which is also solved analytically (these examples are 'designed' to approach the boundary of ellipticity, without the problems connected with the emergence of 'early' bifurcation modes, so that shear band modes are revealed). Finally, we quantify in Section 7 the numerical performance of the approach.

2. Incremental governing equations

We refer here to the Biot [8] constitutive framework (see also [11,42]), in which the increment of nominal stress $\dot{t}_{ij}$ is related to the gradient of incremental displacement $v_{l,k}$, satisfying incompressibility

$$v_{i,i} = 0, \tag{1}$$

and to the in-plane hydrostatic stress increment (expressed in the Cauchy and nominal versions)

$$\dot{p} = \frac{\dot{\sigma}_1 + \dot{\sigma}_2}{2}, \quad \dot{\pi} = \frac{\dot{t}_{11} + \dot{t}_{22}}{2} = \dot{p} - \frac{\sigma_1 - \sigma_2}{2} v_{1,1}, \tag{2}$$

where σ_1 and σ_2 are the principal Cauchy stress components, through a fourth-order tensor $\mathbb{K}$, such that

$$\dot{t}_{ij} = \mathbb{K}_{ijkl} v_{l,k} + \dot{p}\delta_{ij} = \widetilde{\mathbb{K}}_{ijkl} v_{l,k} + \dot{\pi}\delta_{ij}. \tag{3}$$

Tensor $\mathbb{K}_{ijkl}$ is defined as a function of the deviatoric and mean components of pre-stress

$$\sigma = \sigma_1 - \sigma_2, \quad p = \frac{\sigma_1 + \sigma_2}{2}, \tag{4}$$

as follows:

$$\begin{aligned}
&\mathbb{K}_{1111} = \mu_* - \frac{\sigma}{2} - p, \quad \mathbb{K}_{1122} = -\mu_*, \quad \mathbb{K}_{1112} = \mathbb{K}_{1121} = 0,\\
&\mathbb{K}_{2211} = -\mu_*, \quad \mathbb{K}_{2222} = \mu_* + \frac{\sigma}{2} - p, \quad \mathbb{K}_{2212} = \mathbb{K}_{2221} = 0,\\
&\mathbb{K}_{1212} = \mu + \frac{\sigma}{2}, \quad \mathbb{K}_{1221} = \mathbb{K}_{2112} = \mu - p, \quad \mathbb{K}_{2121} = \mu - \frac{\sigma}{2},
\end{aligned} \tag{5}$$

and $\widetilde{\mathbb{K}}_{ijkl}$ coincides with $\mathbb{K}_{ijkl}$ except for

$$\widetilde{\mathbb{K}}_{1111} = \widetilde{\mathbb{K}}_{2222} = \mu_* - p. \tag{6}$$

The equations of motion are

$$\dot{t}_{ij,i} + \dot{f}_j = \rho v_{j,tt}, \tag{7}$$

where $\dot{f}_j$ is the dynamic, incremental body force, ρ is the mass density, and pedex $,t$ denotes partial derivative with respect to the time variable. Under the time-harmonic assumption that for every function f of space $\mathbf{x}$ and time t

$$f(\mathbf{x}, t) = \hat{f}(\mathbf{x}) e^{-i\Omega t}, \tag{8}$$

in which Ω is the circular frequency, Eqs. (7) yield

$$\begin{aligned}
&(2\mu_* - p)v_{1,11} + (\mu - p)v_{2,12} + \left(\mu - \frac{\sigma}{2}\right)v_{1,22} = -\dot{\pi}_{,1} - \rho\Omega^2 v_1,\\
&(2\mu_* - p)v_{2,22} + (\mu - p)v_{1,21} + \left(\mu + \frac{\sigma}{2}\right)v_{2,11} = -\dot{\pi}_{,2} - \rho\Omega^2 v_2,
\end{aligned} \tag{9}$$

where all quantities become solely functions of space. Introducing now the stream function

$$v_1 = \psi_{,2}, \quad v_2 = -\psi_{,1}, \tag{10}$$

Eqs. (9) provide the well-known scalar equations:

$$\begin{aligned}
\dot{\pi}_{,11} + \dot{\pi}_{,22} = -2(\mu_* - \mu)(\psi_{,2111} - \psi_{,1222}) + \frac{\sigma}{2}(\psi_{,2111} + \psi_{,1222}), \quad &\left(\mu + \frac{\sigma}{2}\right)\psi_{,1111} + 2(2\mu_* - \mu)\psi_{,1122} + \left(\mu - \frac{\sigma}{2}\right)\psi_{,2222}\\
&= \rho\Omega^2(\psi_{,11} + \psi_{,22}).
\end{aligned} \tag{11}$$

The second of Eqs. (11) yields the regime classification, which – as noticed in [6] – remains identical to the quasi-static case. In particular, the analysis in this paper will be restricted to the elliptic imaginary (EI) or complex (EC) regimes, for which the parameters:

$$\left.\begin{array}{l}\gamma_1\\ \gamma_2\end{array}\right\} = \frac{1-2\dfrac{\mu_*}{\mu}\pm\sqrt{\Delta}}{1+k}, \quad \Delta = k^2 - 4\frac{\mu_*}{\mu} + 4\left(\frac{\mu_*}{\mu}\right)^2, \tag{12}$$

both real and negative in EI and a conjugate pair in EC, depend on the dimensionless pre-stress parameter

$$k = \frac{\sigma}{2\mu} = \frac{\lambda_1^2-\lambda_2^2}{\lambda_1^2+\lambda_2^2}, \tag{13}$$

where the latter equality holds true when an elastic potential exists and expresses k as a function of the in-plane pre-stretches λ_1 and λ_2. In addition to k, we will also make use of the dimensionless parameter χ defining the hydrostatic component of pre-stress as

$$\chi = \frac{p}{\mu} = \frac{\sigma_1+\sigma_2}{2\mu}. \tag{14}$$

3. The dynamic, time-harmonic Green's functions

The time-harmonic Green's function for the stream function, found in [6], is defined as a function of the sin integral and cos integral functions

$$\mathrm{Si}(\mathrm{x}) = \int_0^x \frac{\sin t}{t}\mathrm{d}t, \quad \mathrm{Ci}(\mathrm{x}) = \gamma + \log x + \int_0^x \frac{\cos t - 1}{t}\mathrm{d}t, \tag{15}$$

where γ is the Euler gamma constant, in the following form

$$\psi^g = -\frac{1}{2\pi^2\rho\Omega c}\int_0^\pi \frac{\sin(\alpha+\theta-\delta_{2g}\pi/2)}{\Lambda(\alpha+\theta)}\,\Xi\left(\hat{r}\frac{\cos\alpha}{\sqrt{\Lambda(\alpha+\theta)}}\right)\mathrm{d}\alpha, \tag{16}$$

where

$$\hat{r} = \frac{\Omega r}{c} \quad \text{and} \quad \theta = \tan^{-1}\frac{x_2}{x_1}, \tag{17}$$

with $r = |\mathbf{x}|$, are dimensionless polar coordinates,

$$c = \sqrt{\frac{\mu(1+k)}{\rho}}, \tag{18}$$

is the propagation velocity of a transverse wave travelling parallel to x_1-axis, and

$$\Lambda(\alpha) = \sin^4\alpha(\cot^2\alpha-\gamma_1)(\cot^2\alpha-\gamma_2) > 0, \tag{19}$$

$$\Xi(x) = \sin x\mathrm{Ci}(|x|) - \cos x\mathrm{Si}(\mathrm{x}) - \mathrm{i}\frac{\pi}{2}\sin x, \tag{20}$$

with $\mathrm{i} = \sqrt{-1}$.

Note that $\Lambda(\alpha)$ is always strictly positive in the elliptic regime; moreover,

$$\Lambda(0) = \Lambda(\pi) = 1, \quad \Lambda(\pi/2) = \Lambda(3\pi/2) = \gamma_1\gamma_2 = \frac{1-k}{1+k}; \tag{21}$$

finally, $\Lambda(\alpha) = 1$ in the special case when the incremental response becomes isotropic, $k = 0$ and $\mu = \mu_*$.

In terms of incremental displacement, the Green's function, enjoying the usual symmetry $v_1^2 = v_2^1$, and defined in the dimensionless polar coordinates, is

$$\begin{aligned} v_g^i(r,\theta) = -\frac{(2\delta_{ig}-1)}{2\pi^2\mu(1+k)}\Bigg[&(\log\hat{r}+\gamma)\int_0^\pi K_i^g(\alpha+\theta)\cos(\hat{r}\xi(\alpha,\alpha+\theta))\mathrm{d}\alpha + \int_0^{\frac{\pi}{2}}\log(\xi(\alpha,\alpha+\theta))K_i^g(\alpha+\theta)\cos(\hat{r}\xi(\alpha,\alpha+\theta))\mathrm{d}\alpha \\ &+ (2\delta_{ig}-1)\int_0^{\frac{\pi}{2}}\log(\xi(\alpha,\alpha-\theta))K_i^g(\alpha-\theta)\cos(\hat{r}\xi(\alpha,\alpha-\theta))\mathrm{d}\alpha + \int_0^\pi K_i^g(\alpha+\theta)\Im(\hat{r}\xi(\alpha,\alpha+\theta))\mathrm{d}\alpha \\ &-\mathrm{i}\frac{\pi}{2}\int_0^\pi K_i^g(\alpha+\theta)\cos(\hat{r}\xi(\alpha,\alpha+\theta))\mathrm{d}\alpha\Bigg], \end{aligned} \tag{22}$$

where

$$\xi(\alpha,\beta)=\frac{\cos\alpha}{\sqrt{\Lambda(\beta)}},\quad K_i^g(\alpha)=\frac{\sin\left(\alpha+\frac{\pi}{2}\delta_{i2}\right)\sin\left(\alpha+\frac{\pi}{2}\delta_{g2}\right)}{\Lambda(\alpha)},\tag{23}$$

and function

$$\Im(x)=\cos x\int_0^x\frac{\cos t-1}{t}\mathrm{d}t+\sin x\,\mathrm{Si}(\mathrm{x}),\tag{24}$$

is non-singular.

3.1. The gradient of incremental displacements

The gradient of incremental displacements is instrumental to the formulation of the boundary element technique. This can be obtained from Eq. (22), employing the derivative rule:

$$\begin{aligned}\frac{\partial v_i^g}{\partial x_1}&=\cos\theta\frac{\partial v_i^g}{\partial r}-\frac{\sin\theta}{r}\frac{\partial v_i^g}{\partial\theta},\\ \frac{\partial v_i^g}{\partial x_2}&=\sin\theta\frac{\partial v_i^g}{\partial r}+\frac{\cos\theta}{r}\frac{\partial v_i^g}{\partial\theta},\end{aligned}\tag{25}$$

and resulting in

$$\begin{aligned}v^s_{g,k}=-\frac{(2\delta_{sg}-1)}{2\pi^2\mu(1+k)}\Bigg\{&v^{s*}_{g,k}-\left(\log\hat r+\gamma-\mathrm{i}\frac{\pi}{2}\right)\Bigg[\int_0^\pi K_s^g(\alpha+\theta)\sin(\hat r\xi(\alpha,\alpha+\theta))\frac{\Omega}{c}\xi(\alpha,\alpha+\theta)\zeta(\alpha+\theta,\theta-\delta_{2k}\pi/2)\mathrm{d}\alpha\\ &+\frac{\sin(\theta-\delta_{2k}\pi/2)}{r}\int_0^\pi\Sigma(\alpha+\theta-\delta_{2s}\pi/2,\alpha+\theta)\cos(\hat r\xi(\alpha,\alpha+\theta))\mathrm{d}\alpha\Bigg]\\ &-\int_0^{\frac{\pi}{2}}\log\xi(\alpha,\alpha+\theta)K_s^g(\alpha+\theta)\sin(\hat r\xi(\alpha,\alpha+\theta))\frac{\Omega}{c}\xi(\alpha,\alpha+\theta)\zeta(\alpha+\theta,\theta-\delta_{2k}\pi/2)\mathrm{d}\alpha\\ &+\int_0^{\frac{\pi}{2}}\log\xi(\alpha,\alpha-\theta)K_s^g(\alpha-\theta)\sin(\hat r\xi(\alpha,\alpha-\theta))\frac{\Omega}{c}\xi(\alpha,\alpha-\theta)\zeta(\alpha-\theta,-\theta-\delta_{2k}\pi/2)\mathrm{d}\alpha\\ &+\int_0^\pi K_s^g(\alpha+\theta)\wp(\hat r\xi(\alpha,\alpha+\theta))\frac{\Omega}{c}\xi(\alpha,\alpha+\theta)\zeta(\alpha+\theta,\theta-\delta_{2k}\pi/2)\mathrm{d}\alpha\Bigg\},\end{aligned}\tag{26}$$

where the strongly singular term $v^{s*}_{g,k}$ is defined as

$$\begin{aligned}v^{s*}_{g,k}=\frac{1}{r}\Bigg\{&\cos(\theta-\delta_{2k}\pi/2)\int_0^\pi K_s^g(\alpha+\theta)\cos(\hat r\xi(\alpha,\alpha+\theta))\mathrm{d}\alpha+\sin(\theta-\delta_{2k}\pi/2)\\ &\times\int_0^{\frac{\pi}{2}}\Bigg[\frac{\Lambda'(\alpha+\theta)}{2\Lambda(\alpha+\theta)}K_s^g(\alpha+\theta)\cos(\hat r\xi(\alpha,\alpha+\theta))-\log(\xi(\alpha,\alpha+\theta)\Sigma(\alpha+\theta-\delta_{2s}\pi/2,\alpha+\theta)\cos(\hat r\xi(\alpha,\alpha+\theta))\\ &+(1-2\delta_{1g}\delta_{1s})\left(\frac{\Lambda'(\alpha-\theta)}{2\Lambda(\alpha-\theta)}K_s^g(\alpha-\theta)\cos(\hat r\xi(\alpha,\alpha-\theta))-\log\xi(\alpha,\alpha-\theta)\Sigma(\alpha-\theta-\delta_{2s}\pi/2,\alpha+\theta)\cos(\hat r\xi(\alpha,\alpha-\theta))\right)\Bigg]\mathrm{d}\alpha\\ &-\int_0^\pi K_s^g(\alpha+\theta)(\cos(\hat r\xi(\alpha,\alpha+\theta))-1)\zeta(\alpha+\theta,\theta-\delta_{2k}\pi/2)\mathrm{d}\alpha-\sin(\theta-\delta_{2k}\pi/2)\\ &\times\int_0^\pi\Sigma(\alpha+\theta-\delta_{2s}\pi/2,\alpha+\theta)\Im(\hat r\xi(\alpha,\alpha+\theta))\mathrm{d}\alpha\Bigg\},\end{aligned}\tag{27}$$

with the following notation

$$\Lambda'(\beta)=\frac{\partial\Lambda(\beta)}{\partial\beta}=\sin(2\beta)[(2\gamma_1\gamma_2+\gamma_1+\gamma_2)\sin^2\beta-(2+\gamma_1+\gamma_2)\cos^2\beta],\tag{28}$$

$$\Sigma(\alpha,\beta)=\frac{\sin\alpha[2\cos\alpha\Lambda(\beta)-\sin\alpha\Lambda'(\beta)]}{\Lambda^2(\beta)},\tag{29}$$

$$\zeta(\alpha,\theta)=\cos\theta+\frac{\sin\theta}{2}\frac{\Lambda'(\alpha)}{\Lambda(\alpha)},\tag{30}$$

and, finally

$$\wp(x)=-\sin x\int_0^x\frac{\cos t-1}{t}\mathrm{d}t+\cos x\,\mathrm{Si}(\mathrm{x}).\tag{31}$$

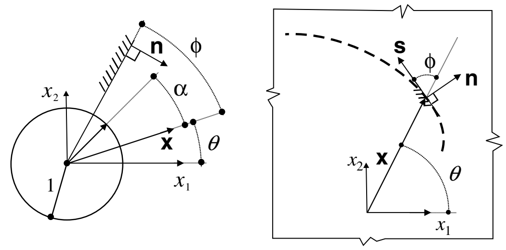

Fig. 1. Reference system, vectors $\boldsymbol{\omega}$, $\mathbf{x}$, $\mathbf{n}$, and angles θ, α and ϕ (left). Geometric representation of angles θ and ϕ (right).

The plane wave expansion of the gradient of incremental displacement is

$$v^g_{j,k} = -\frac{1}{4\pi^2}\oint_{|\boldsymbol{\omega}|=1} \tilde{v}^g_{j,k}(\boldsymbol{\omega}\cdot\mathbf{x})\mathrm{d}\omega, \tag{32}$$

where the unit vector $\boldsymbol{\omega}$ traces the unit circle in the x_1–x_2 plane and is defined as in Fig. 1 and

$$\tilde{v}^g_{j,k} = \omega_k \frac{\delta_{jg} - \omega_j\omega_g}{L(\boldsymbol{\omega})}\left[\frac{1}{\boldsymbol{\omega}\cdot\mathbf{x}} - \eta\Xi(\eta\boldsymbol{\omega}\cdot\mathbf{x})\right], \tag{33}$$

in which

$$L(\boldsymbol{\omega}) = \mu(1+k)\omega_2^4\left(\frac{\omega_1^2}{\omega_2^2} - \gamma_1\right)\left(\frac{\omega_1^2}{\omega_2^2} - \gamma_2\right) > 0, \tag{34}$$

and

$$\eta = \Omega\sqrt{\frac{\rho}{L(\boldsymbol{\omega})}}. \tag{35}$$

A comparison of Eq. (33) with the gradient of $\tilde{v}^g_i$ in the quasi-static case (see [5] their Eq. (31)) shows that the singular term in Eq. (33) is identical to the quasi-static counterpart, so that we can write

$$\tilde{v}^g_{j,k} = (\tilde{v}^g_{j,k})_{\text{static}} - \omega_k \frac{\delta_{jg} - \omega_j\omega_g}{L(\boldsymbol{\omega})}\eta\Xi(\eta\boldsymbol{\omega}\cdot\mathbf{x}), \tag{36}$$

an expression which permits a systematic separation between the quasi-static and the dynamic terms.

3.2. The Green's function for in-plane incremental hydrostatic stress

Taking the plane wave expansion of the in-plane incremental hydrostatic stress

$$\dot{\pi}^g(\mathbf{x}) = -\frac{1}{4\pi^2}\oint_{|\boldsymbol{\omega}|=1} \tilde{\pi}^g(\boldsymbol{\omega}\cdot\mathbf{x})\mathrm{d}\omega, \tag{37}$$

and substituting into Eq. $(11)_1$, we get

$$\tilde{\pi}^g = \frac{\omega_g}{\boldsymbol{\omega}\cdot\mathbf{x}} + (\delta_{2g} - \delta_{1g})\frac{\omega_g(1-\omega_g^2)}{L(\boldsymbol{\omega})}\left[2(\mu_* - \mu)(\omega_1^2 - \omega_2^2) - \frac{\sigma}{2}\right]\left[\frac{1}{\boldsymbol{\omega}\cdot\mathbf{x}} - \eta\Xi(\eta\boldsymbol{\omega}\cdot\mathbf{x})\right], \tag{38}$$

where Ξ is given by Eq. (20).

An alternative form of Eq. (38), useful for subsequent calculations, is

$$\tilde{\pi}^g = \omega_g\eta\Xi(\eta\boldsymbol{\omega}\cdot\mathbf{x}) + \omega_g\frac{(2\mu_* - \mu)(1-\omega_g^2) + [\mu - (\delta_{2g} - \delta_{1g})\sigma/2]\omega_g^2}{L(\boldsymbol{\omega})}\left[\frac{1}{\boldsymbol{\omega}\cdot\mathbf{x}} - \eta\Xi(\eta\boldsymbol{\omega}\cdot\mathbf{x})\right]. \tag{39}$$

A comparison between Eqs. (39) or (38) and the quasi-static counterpart (given in [5], their Eq. (44)) reveals that the singular terms are again identical, so that we may write

$$\tilde{\pi}^g = (\tilde{\pi}^g)_{\text{static}} + \omega_g\eta\Xi(\eta\boldsymbol{\omega}\cdot\mathbf{x})\left[1 - \frac{(2\mu_* - \mu)(1-\omega_g^2) + [\mu - (\delta_{2g} - \delta_{1g})\sigma/2]\omega_g^2}{L(\boldsymbol{\omega})}\right], \tag{40}$$

an equation representing the complement to Eq. (36) for determining the Green's functions for the incremental stress components.

Employing Eq. (38) in (37), the Green's function for the incremental hydrostatic stress is obtained in the following form

$$\dot{\pi}^g = (\dot{\pi}^g)_{\text{static}} - \frac{\Omega}{2\pi^2(1+k)c}\int_0^{\pi}\frac{\tilde{K}_g(\alpha+\theta)}{\sqrt{\Lambda(\alpha+\theta)}}\quad \Xi\left(\frac{\Omega r}{c}\frac{\cos\alpha}{\sqrt{\Lambda(\alpha+\theta)}}\right)\mathrm{d}\alpha, \tag{41}$$

where the quasi-static Green's function, containing the singular terms, is

$$(\dot{\pi}^g)_{\text{static}} = -\frac{1}{2\pi r}\left\{\cos\left[\theta - \delta_{2g}\frac{\pi}{2}\right] + \frac{1}{\pi(1+k)}\int_0^{\pi}\frac{\widetilde{K}_g(\alpha+\theta)}{\cos\alpha}\mathrm{d}\alpha\right\}, \tag{42}$$

in which

$$\widetilde{K}_g(\alpha) = K_g^g(\alpha)\left[2\left(\frac{\mu_*}{\mu}-1\right)(2\cos^2\alpha - 1) - k\right]\cos\left[\alpha + \delta_{2g}\frac{\pi}{2}\right]. \tag{43}$$

Note that the Green's function in terms of Cauchy in plane pressure increment $\dot{p}^g$ can be obtained from Eq. (41) by using

$$\dot{p}^g = \dot{\pi}^g - \frac{\sigma}{2}v_{1,1}^g. \tag{44}$$

3.3. The Green's functions for incremental nominal stresses

From the knowledge of the Green's function for gradient of incremental displacement (26) and hydrostatic pressure (41), the Green's function for incremental nominal stresses can be obtained using the constitutive laws (3) in the form:

$$\begin{aligned} \dot{t}_{11}^g &= (2\mu_* - p)v_{1,1}^g + \dot{\pi}^g, & \dot{t}_{12}^g &= (\mu - p)v_{1,2}^g + \left(\mu + \frac{\sigma}{2}\right)v_{2,1}^g, \\ \dot{t}_{21}^g &= (\mu - p)v_{2,1}^g + \left(\mu - \frac{\sigma}{2}\right)v_{1,2}^g, & \dot{t}_{22}^g &= (2\mu_* - p)v_{2,2}^g + \dot{\pi}^g. \end{aligned} \tag{45}$$

4. The Green's functions for incremental applied tractions

The Green's functions for incremental applied nominal tractions τ_j^g at a boundary of unit outward normal n_i can be evaluated through substitution of Eqs. (45) into

$$\tau_j^g = \dot{t}_{ij}^g n_i. \tag{46}$$

However, the Green's function for incremental applied nominal tractions are crucial in the development of the boundary element technique, since these appear in the boundary integral equations (that will be introduced later).

We present now a new derivation of the Green's functions for incremental applied nominal tractions which provides expressions equivalent to those obtained by substitution of Eqs. (45) into Eq. (46), but showing important features, which remain otherwise unrevealed. These are:

- static and dynamic contributions to the Green's functions for incremental applied tractions turn out to be uncoupled, in the form

$$\tau_j^g = \tau_{j\,\text{static}}^g + \tau_{j\,\text{dynamic}}^g; \tag{47}$$

- while the static contributions are strongly singular, the dynamic contributions are not;
- let us define ϕ as the angle between the position vector $\mathbf{x}$ and the material surface (of unit normal $\mathbf{n}$, and unit tangent $\mathbf{s}$ oriented counterclockwise) on which the traction acts (Fig. 1). When $\phi = 0$ or $\phi = \pi$, the components $\tau_{g\,\text{static}}^g$ *are null*, while $\tau_{2\,\text{static}}^1$ and $\tau_{1\,\text{static}}^2$ depend in closed form expressions on $r = |\mathbf{x}|$ *only*. This property[3] will be crucially advantageous in the evaluation of strongly singular integrals at piecewise-rectilinear boundaries.

To obtain the above-mentioned representation of the Green's functions for incremental applied nominal tractions, we begin with the plane wave expansion of the nominal traction

$$\tau_j^g(\mathbf{x}) = -\frac{1}{4\pi^2}\oint_{|\boldsymbol{\omega}|=1}\tilde{\tau}_j^g(\boldsymbol{\omega}\cdot\mathbf{x})\mathrm{d}\omega, \tag{48}$$

[3] The dependence of the traction only on r when $\phi = 0$ was numerically checked in [11]. Now this property will be proved.

so that the components of the nominal traction increments become using Eqs. (33) and (39) into Eq. (46)

$$\begin{aligned}
\tilde{\tau}_1^1 &= \{[(2\mu_* - p)\omega_1\omega_2^2 + \omega_1((2\mu_* - \mu)\omega_2^2 + (\mu + \sigma/2)\omega_1^2)]n_1 - [(\mu - p)\omega_1^2\omega_2 - (\mu - \sigma/2)\omega_2^3]n_2\} \\
&\quad \frac{1}{L(\boldsymbol{\omega})}\left[\frac{1}{\boldsymbol{\omega}\cdot\mathbf{x}} - \eta\Xi(\eta\boldsymbol{\omega}\cdot\mathbf{x})\right] + \omega_1 n_1 \eta\Xi(\eta\boldsymbol{\omega}\cdot\mathbf{x}), \\
\tilde{\tau}_2^2 &= \{[(2\mu_* - p)\omega_1^2\omega_2 + \omega_2((2\mu_* - \mu)\omega_1^2 + (\mu - \sigma/2)\omega_2^2)]n_2 - [(\mu - p)\omega_1\omega_2^2 - (\mu + \sigma/2)\omega_1^3]n_1\} \\
&\quad \frac{1}{L(\boldsymbol{\omega})}\left[\frac{1}{\boldsymbol{\omega}\cdot\mathbf{x}} - \eta\Xi(\eta\boldsymbol{\omega}\cdot\mathbf{x})\right] + \omega_2 n_2 \eta\Xi(\eta\boldsymbol{\omega}\cdot\mathbf{x}), \\
\tilde{\tau}_2^1 &= \{[-(2\mu_* - p)\omega_1\omega_2^2 + \omega_1((2\mu_* - \mu)\omega_2^2 + (\mu + \sigma/2)\omega_1^2)]n_2 + [(\mu - p)\omega_2^3 - (\mu + \sigma/2)\omega_1^2\omega_2]n_1\} \\
&\quad \frac{1}{L(\boldsymbol{\omega})}\left[\frac{1}{\boldsymbol{\omega}\cdot\mathbf{x}} - \eta\Xi(\eta\boldsymbol{\omega}\cdot\mathbf{x})\right] + \omega_1 n_2 \eta\Xi(\eta\boldsymbol{\omega}\cdot\mathbf{x}), \\
\tilde{\tau}_1^2 &= \{[-(2\mu_* - p)\omega_1^2\omega_2 + \omega_2((2\mu_* - \mu)\omega_1^2 + (\mu - \sigma/2)\omega_2^2)]n_1 + [(\mu - p)\omega_1^3 - (\mu - \sigma/2)\omega_2^2\omega_1]n_2\} \\
&\quad \frac{1}{L(\boldsymbol{\omega})}\left[\frac{1}{\boldsymbol{\omega}\cdot\mathbf{x}} - \eta\Xi(\eta\boldsymbol{\omega}\cdot\mathbf{x})\right] + \omega_2 n_1 \eta\Xi(\eta\boldsymbol{\omega}\cdot\mathbf{x}).
\end{aligned} \tag{49}$$

Application of the plane wave expansion (48) yields the following form of the components of the nominal traction increments

$$\begin{aligned}
\tau_1^1 &= \tau_{1\,\text{static}}^1 - \frac{1}{4\pi^2}\oint_{|\boldsymbol{\omega}|=1} \eta\Xi(\eta\boldsymbol{\omega}\cdot\mathbf{x})\left\{\omega_1 n_1 - \frac{1}{L(\boldsymbol{\omega})}\left[\left(2(2\mu_* - \mu)\omega_1\omega_2^2 + \left(\mu + \frac{\sigma}{2}\right)\omega_1^3\right)n_1 + \left(\mu - \frac{\sigma}{2}\right)\omega_2^3 n_2\right.\right. \\
&\quad \left.\left. + (\mu - p)\omega_1\omega_2(\omega_2 n_1 - \omega_1 n_2)\right]\right\}\mathrm{d}\omega, \\
\tau_2^2 &= \tau_{2\,\text{static}}^2 - \frac{1}{4\pi^2}\oint_{|\boldsymbol{\omega}|=1} \eta\Xi(\eta\boldsymbol{\omega}\cdot\mathbf{x})\left\{\omega_2 n_2 - \frac{1}{L(\boldsymbol{\omega})}\left[\left(2(2\mu_* - \mu)\omega_1^2\omega_2 + \left(\mu - \frac{\sigma}{2}\right)\omega_2^3\right)n_2\right.\right. \\
&\quad \left.\left. + \left(\mu + \frac{\sigma}{2}\right)\omega_1^3 n_1 - (\mu - p)\omega_1\omega_2(\omega_2 n_1 - \omega_1 n_2)\right]\right\}\mathrm{d}\omega, \\
\tau_2^1 &= \tau_{2\,\text{static}}^1 - \frac{1}{4\pi^2}\oint_{|\boldsymbol{\omega}|=1} \eta\Xi(\eta\boldsymbol{\omega}\cdot\mathbf{x})\left\{\omega_1 n_2 - \left[(\mu - p)\omega_2^2 - \left(\mu + \frac{\sigma}{2}\right)\omega_1^2\right]\frac{\omega_2 n_1 - \omega_1 n_2}{L(\boldsymbol{\omega})}\right\}\mathrm{d}\omega, \\
\tau_1^2 &= \tau_{1\,\text{static}}^2 - \frac{1}{4\pi^2}\oint_{|\boldsymbol{\omega}|=1} \eta\Xi(\eta\boldsymbol{\omega}\cdot\mathbf{x})\left\{\omega_2 n_1 + \left[(\mu - p)\omega_1^2 - \left(\mu - \frac{\sigma}{2}\right)\omega_2^2\right]\frac{\omega_2 n_1 - \omega_1 n_2}{L(\boldsymbol{\omega})}\right\}\mathrm{d}\omega,
\end{aligned} \tag{50}$$

where the $\tau_{i\,\text{static}}^j$ are the quasi-static tractions given by

$$\begin{aligned}
\tau_{1\,\text{static}}^1 &= -\frac{1}{4\pi^2}\oint_{|\boldsymbol{\omega}|=1}\left\{\frac{n_1}{\omega_1} - \left[\left(\mu - \frac{\sigma}{2}\right)\frac{\omega_2}{\omega_1} - \left(2\mu - \frac{\sigma}{2} - p\right)\omega_1\omega_2\right]\frac{\omega_2 n_1 - \omega_1 n_2}{L(\boldsymbol{\omega})}\right\}\frac{\mathrm{d}\omega}{\boldsymbol{\omega}\cdot\mathbf{x}}, \\
\tau_{2\,\text{static}}^2 &= -\frac{1}{4\pi^2}\oint_{|\boldsymbol{\omega}|=1}\left\{\frac{n_2}{\omega_2} + \left[\left(\mu + \frac{\sigma}{2}\right)\frac{\omega_1}{\omega_2} - \left(2\mu + \frac{\sigma}{2} - p\right)\omega_1\omega_2\right]\frac{\omega_2 n_1 - \omega_1 n_2}{L(\boldsymbol{\omega})}\right\}\frac{\mathrm{d}\omega}{\boldsymbol{\omega}\cdot\mathbf{x}}, \\
\tau_{2\,\text{static}}^1 &= -\frac{1}{4\pi^2}\oint_{|\boldsymbol{\omega}|=1}\left[(\mu - p)\omega_2^2 - \left(\mu + \frac{\sigma}{2}\right)\omega_1^2\right]\frac{\omega_2 n_1 - \omega_1 n_2}{L(\boldsymbol{\omega})}\frac{\mathrm{d}\omega}{\boldsymbol{\omega}\cdot\mathbf{x}}, \\
\tau_{1\,\text{static}}^2 &= -\frac{1}{4\pi^2}\oint_{|\boldsymbol{\omega}|=1}\left[-(\mu - p)\omega_1^2 + \left(\mu - \frac{\sigma}{2}\right)\omega_2^2\right]\frac{\omega_2 n_1 - \omega_1 n_2}{L(\boldsymbol{\omega})}\frac{\mathrm{d}\omega}{\boldsymbol{\omega}\cdot\mathbf{x}}.
\end{aligned} \tag{51}$$

Assuming that the normal to the material surface to which the traction is referred can be expressed in terms of the angle ϕ measured from θ (see Fig. 1) as

$$n_1 = \sin(\phi + \theta), \quad n_2 = -\cos(\phi + \theta), \tag{52}$$

the dynamic contributions in Eqs. (50) can be further re-written leading to the following expressions for the Green incremental tractions

$$
\begin{aligned}
\tau_1^1 &= \tau_{1\,\text{static}}^1 - \frac{\Omega}{2\pi^2 c}\int_0^\pi \frac{\Xi(\hat{r}\xi(\alpha,\alpha+\theta))}{\sqrt{\Lambda(\alpha+\theta)}}\left\{\cos(\alpha+\theta)\sin(\phi+\theta) - \frac{1}{(1+k)\Lambda(\alpha+\theta)}\right.\\
&\quad\left[\left(2\left(2\frac{\mu_*}{\mu}-1\right)\cos(\alpha+\theta)\sin^2(\alpha+\theta)+(1+k)\cos^3(\alpha+\theta)\right)\sin(\phi+\theta)\right.\\
&\quad\left.\left.-(1-k)\sin^3(\alpha+\theta)\cos(\phi+\theta)+(1-\chi)\cos(\alpha+\theta)\sin(\alpha+\theta)\cos(\alpha-\phi)\right]\right\}\mathrm{d}\alpha,\\
\tau_2^2 &= \tau_{2\,\text{static}}^2 + \frac{\Omega}{2\pi^2 c}\int_0^\pi \frac{\Xi(\hat{r}\xi(\alpha,\alpha+\theta))}{\sqrt{\Lambda(\alpha+\theta)}}\left\{\sin(\alpha+\theta)\cos(\phi+\theta) - \frac{1}{(1+k)\Lambda(\alpha+\theta)}\right.\\
&\quad\left[\left(2\left(2\frac{\mu_*}{\mu}-1\right)\cos^2(\alpha+\theta)\sin(\alpha+\theta)+(1-k)\sin^3(\alpha+\theta)\right)\cos(\phi+\theta)\right.\\
&\quad\left.\left.-(1+k)\cos^3(\alpha+\theta)\sin(\phi+\theta)+(1-\chi)\cos(\alpha+\theta)\sin(\alpha+\theta)\cos(\alpha-\phi)\right]\right\}\mathrm{d}\alpha,\\
\tau_2^1 &= \tau_{2\,\text{static}}^1 + \frac{\Omega}{2\pi^2 c}\int_0^\pi \frac{\Xi(\hat{r}\xi(\alpha,\alpha+\theta))}{\sqrt{\Lambda(\alpha+\theta)}}\left\{\cos(\alpha+\theta)\cos(\phi+\theta) + \frac{\cos(\alpha-\phi)}{(1+k)\Lambda(\alpha+\theta)}\right.\\
&\quad\left.[(1-\chi)\sin^2(\alpha+\theta)-(1+k)\cos^2(\alpha+\theta)]\right\}\mathrm{d}\alpha,\\
\tau_1^2 &= \tau_{1\,\text{static}}^2 - \frac{\Omega}{2\pi^2 c}\int_0^\pi \frac{\Xi(\hat{r}\xi(\alpha,\alpha+\theta))}{\sqrt{\Lambda(\alpha+\theta)}}\left\{\sin(\alpha+\theta)\sin(\phi+\theta) + \frac{\cos(\alpha-\phi)}{(1+k)\Lambda(\alpha+\theta)}\right.\\
&\quad\left.[(1-\chi)\cos^2(\alpha+\theta)-(1-k)\sin^2(\alpha+\theta)]\right\}\mathrm{d}\alpha.
\end{aligned}
\tag{53}
$$

The strongly singular static contributions to the Green incremental tractions will be analysed in the subsection below.

4.1. The quasi-static incremental tractions

Calculations deferred to Appendix A show that the incremental tractions in the quasi-static approximation (51) become

$$
\begin{aligned}
\tau_{1\,\text{static}}^1 &= \frac{\sin\phi}{2\pi^2(1+k)r}\left\{(1-k)\,⨍_0^\pi \frac{\tan(\alpha+\theta)\tan\alpha}{\Lambda(\alpha+\theta)}\mathrm{d}\alpha - (2-k-\chi)\,⨍_0^\pi \frac{\sin(\alpha+\theta)\cos(\alpha+\theta)\tan\alpha}{\Lambda(\alpha+\theta)}\mathrm{d}\alpha\right\},\\
\tau_{2\,\text{static}}^2 &= -\frac{\sin\phi}{2\pi^2 r}\left\{⨍_0^\pi \frac{\cot(\alpha+\theta)\tan\alpha}{\Lambda(\alpha+\theta)}\mathrm{d}\alpha - \frac{2+k-\chi}{1+k} - ⨍_0^\pi \frac{\sin(\alpha+\theta)\cos(\alpha+\theta)\tan\alpha}{\Lambda(\alpha+\theta)}\mathrm{d}\alpha\right\},\\
\tau_{2\,\text{static}}^1 &= \frac{\cos\phi}{2\pi(1+k)r}\left(\frac{1-\chi}{\gamma_1\sqrt{-\gamma_2}+\gamma_2\sqrt{-\gamma_1}} + \frac{1+k}{\sqrt{-\gamma_2}+\sqrt{-\gamma_1}}\right) - \frac{\sin\phi}{2\pi^2(1+k)r}⨍_0^\pi \frac{\tan\alpha}{\Lambda(\alpha+\theta)}[(1-\chi)\sin^2(\alpha+\theta)\\
&\quad -(1+k)\cos^2(\alpha+\theta)]\mathrm{d}\alpha,\\
\tau_{1\,\text{static}}^2 &= \frac{\cos\phi}{2\pi(1+k)r}\left(\frac{1-\chi}{\sqrt{-\gamma_2}+\sqrt{-\gamma_1}} + \frac{1-k}{\gamma_1\sqrt{-\gamma_2}+\gamma_2\sqrt{-\gamma_1}}\right)\\
&\quad + \frac{\sin\phi}{2\pi^2(1+k)r}⨍_0^\pi \frac{\tan\alpha}{\Lambda(\alpha+\theta)}[(1-\chi)\cos^2(\alpha+\theta)-(1-k)\sin^2(\alpha+\theta)]\mathrm{d}\alpha.
\end{aligned}
\tag{54}
$$

Note that Eqs. $(54)_{1,2}$ can be regularized. In particular, assuming $0<\theta<2\pi$, we obtain (see Appendix B)

$$
\begin{aligned}
\tau_{1\,\text{static}}^1 &= \frac{\sin\phi}{2\pi^2 r}\left\{\cot\theta\log\left|\frac{\beta_1}{\beta_1-\pi}\right| + \int_0^\pi\left[\frac{\gamma_1\gamma_2\tan(\alpha+\theta)\tan\alpha}{\Lambda(\alpha+\theta)} + \frac{\gamma_1\gamma_2\cot\theta}{(\pi/2-\alpha)\Lambda(\pi/2+\theta)} - \frac{\cot\theta}{\beta_1-\alpha}\right]\mathrm{d}\alpha\right.\\
&\quad\left.-\frac{2-k-\chi}{1+k}\int_0^\pi\left[\frac{\sin(\alpha+\theta)\cos(\alpha+\theta)\tan\alpha}{\Lambda(\alpha+\theta)} + \frac{\cos\theta\sin\theta}{(\pi/2-\alpha)\Lambda(\pi/2+\theta)}\right]\mathrm{d}\alpha\right\},\\
\tau_{2\,\text{static}}^2 &= -\frac{\sin\phi}{2\pi^2 r}\left\{\tan\theta\log\left|\frac{\beta_2}{\beta_2-\pi}\right| + \int_0^\pi\left[\frac{\cot(\alpha+\theta)\tan\alpha}{\Lambda(\alpha+\theta)} + \frac{\tan\theta}{(\pi/2-\alpha)\Lambda(\pi/2+\theta)} - \frac{\tan\theta}{\beta_2-\alpha}\right]\mathrm{d}\alpha\right.\\
&\quad\left.-\frac{2+k-\chi}{1+k}\int_0^\pi\left[\frac{\sin(\alpha+\theta)\cos(\alpha+\theta)\tan\alpha}{\Lambda(\alpha+\theta)} + \frac{\cos\theta\sin\theta}{(\pi/2-\alpha)\Lambda(\pi/2+\theta)}\right]\mathrm{d}\alpha\right\},
\end{aligned}
$$

$$
\begin{aligned}
\tau^1_{2\,\mathrm{static}} &= \frac{\cos\phi}{r}T^1_2 - \frac{\sin\phi}{2\pi^2 r}\int_0^{\pi}\left\{\frac{\tan\alpha}{\Lambda(\alpha+\theta)}\left[\frac{1-\chi}{1+k}\sin^2(\alpha+\theta)-\cos^2(\alpha+\theta)\right]\right.\\
&\quad\left.-\frac{1}{\Lambda(\pi/2+\theta)(\pi/2-\alpha)}\left[\frac{1-\chi}{1+k}\cos^2\theta-\sin^2\theta\right]\right\}\mathrm{d}\alpha,\\
\tau^2_{1\,\mathrm{static}} &= \frac{\cos\phi}{r}T^2_1 + \frac{\sin\phi}{2\pi^2 r}\int_0^{\pi}\left\{\frac{\tan\alpha}{\Lambda(\alpha+\theta)}\left[\frac{1-\chi}{1+k}\cos^2(\alpha+\theta)-\gamma_1\gamma_2\sin^2(\alpha+\theta)\right]\right.\\
&\quad\left.-\frac{1}{\Lambda(\pi/2+\theta)(\pi/2-\alpha)}\left[\frac{1-\chi}{1+k}\sin^2\theta-\gamma_1\gamma_2\cos^2\theta\right]\right\}\mathrm{d}\alpha,
\end{aligned}
\tag{55}
$$

where coefficients

$$
T^1_2 = \frac{1}{2\pi(1+k)}\left(\frac{1-\chi}{\gamma_1\sqrt{-\gamma_2}+\gamma_2\sqrt{-\gamma_1}}+\frac{1+k}{\sqrt{-\gamma_2}+\sqrt{-\gamma_1}}\right),
\tag{56}
$$

$$
T^2_1 = \frac{1}{2\pi(1+k)}\left(\frac{1-\chi}{\sqrt{-\gamma_2}+\sqrt{-\gamma_1}}+\frac{1-k}{\gamma_1\sqrt{-\gamma_2}+\gamma_2\sqrt{-\gamma_1}}\right),
\tag{57}
$$

are independent of r and θ, and angles β_1, β_2 are defined as

$$
\begin{aligned}
\beta_1 &= \frac{\pi}{2}-\theta \quad \text{if } 0<\theta\leqslant\frac{\pi}{2},\\
\beta_1 &= \frac{3\pi}{2}-\theta \quad \text{if } \frac{\pi}{2}\leqslant\theta\leqslant\frac{3\pi}{2},\\
\beta_1 &= \frac{5\pi}{2}-\theta \quad \text{if } \frac{3\pi}{2}\leqslant\theta<2\pi,
\end{aligned}
\tag{58}
$$

$$
\begin{aligned}
\beta_2 &= \pi-\theta \quad \text{if } 0<\theta<\frac{\pi}{2} \quad \text{and} \quad \frac{\pi}{2}<\theta\leqslant\pi,\\
\beta_2 &= 2\pi-\theta \quad \text{if } \pi\leqslant\theta<\frac{3\pi}{2} \quad \text{and} \quad \frac{3\pi}{2}<\theta\leqslant 2\pi.
\end{aligned}
\tag{59}
$$

The simple relationships

$$
\gamma_1\sqrt{-\gamma_2}+\gamma_2\sqrt{-\gamma_1} = \sqrt{\gamma_1\gamma_2}\left(\sqrt{-\gamma_2}+\sqrt{-\gamma_1}\right) = \sqrt{\gamma_1\gamma_2}\sqrt{-\gamma_1-\gamma_2+2\sqrt{\gamma_1\gamma_2}},
\tag{60}
$$

show that the denominators appearing in Eqs. (56) and (57) are always real and positive.

Note that there are four particular cases in which the integrals in Eqs. $(55)_{1,2}$ become hypersingular and have a meaning only in the Hadamard sense. These occur when θ equals 0 or π in Eq. $(55)_1$ or θ equals $\pi/2$ or $3\pi/2$ in Eq. $(55)_2$. In the limits $\theta\to 0$ or $\theta\to\pi$, Eq. $(55)_1$ reduces to

$$
\tau^1_{1\,\mathrm{static}} = \frac{\sin\phi}{2\pi^2 r}\left\{-\frac{4}{\pi}+\int_0^{\pi}\left[\frac{\gamma_1\gamma_2\tan^2\alpha}{\Lambda(\alpha)}-\frac{1}{(\pi/2-\alpha)^2}\right]\mathrm{d}\alpha-\frac{2-k-\chi}{1+k}\int_0^{\pi}\frac{\sin^2\alpha}{\Lambda(\alpha)}\mathrm{d}\alpha\right\},
\tag{61}
$$

while in the limits $\theta\to\pi/2$ or $\theta\to 3\pi/2$, Eq. $(55)_2$ reduces to

$$
\tau^2_{2\,\mathrm{static}} = \frac{\sin\phi}{2\pi^2 r}\left\{-\frac{4}{\pi}+\int_0^{\pi}\left[\frac{\tan^2\alpha}{\Lambda(\alpha+\pi/2)}-\frac{1}{(\pi/2-\alpha)^2}\right]\mathrm{d}\alpha-\frac{2+k-\chi}{1+k}\int_0^{\pi}\frac{\sin^2\alpha}{\Lambda(\alpha)}\mathrm{d}\alpha\right\}.
\tag{62}
$$

In the last two equations, the integrals have been regularized and correspond to the Hadamard finite parts.

Finally, we note that Eqs. (55) can be shown to reduce to the well-known particular case of linear elasticity (reported in Appendix C), when $k=\chi=0$ and $\mu=\mu_*$.

5. Boundary element formulation

5.1. Boundary integral equations

The boundary integral equations at an interior point $\mathbf{y}$ have been obtained by Bigoni and Capuani [6] in the form

$$
v_g(\mathbf{y}) = \int_{\partial B}[\tau_i(\mathbf{x})v_i^g(\mathbf{x},\mathbf{y})-\tau_i^g(\mathbf{x},\mathbf{y})v_i(\mathbf{x})]\mathrm{d}l_x,
\tag{63}
$$

for incremental displacements and

$$\begin{aligned}\dot{p}(\mathbf{y}) = &-\int_{\partial B}\tau_g(\mathbf{x})\dot{p}^g(\mathbf{x},\mathbf{y})\mathrm{d}l_x + \int_{\partial B} n_i(\mathbf{x})v_j(\mathbf{x})\mathbb{K}_{ijkg}\dot{p}^g_{,k}(\mathbf{x},\mathbf{y})\mathrm{d}l_x \\ &-\left(4\mu\mu_* - 4\mu_*^2 + \mu\sigma - 2\mu_*\sigma - \frac{\sigma^2}{2}\right)\int_{\partial B} n_i(\mathbf{x})v_i(\mathbf{x})v^1_{1,11}(\mathbf{x},\mathbf{y})\mathrm{d}l_x + \sigma\left(\mu+\frac{\sigma}{2}\right)\int_{\partial B} n_i(\mathbf{x})v_i(\mathbf{x})v^2_{2,11}(\mathbf{x},\mathbf{y})\mathrm{d}l_x \\ &-\rho\Omega^2\int_{\partial B} n_i(\mathbf{x})v_i(\mathbf{x})W(\mathbf{x},\mathbf{y})\mathrm{d}l_x, \end{aligned} \tag{64}$$

for incremental in-plane hydrostatic stress. Potential W appearing in Eq. (64) takes the form:

$$\begin{aligned} W = &-\frac{\log\hat{r}}{2\pi} - \frac{1}{2\pi^2\mu(1+k)}\left[(\log\hat{r}+\gamma)\int_0^{\pi} F(\alpha+\theta)\cos(\hat{r}\xi(\alpha+\theta))\mathrm{d}\alpha + \int_0^{\frac{\pi}{2}}\log(\xi(\alpha+\theta))F(\alpha+\theta)\cos(\hat{r}\xi(\alpha+\theta))\mathrm{d}\alpha\right. \\ &\left.+\int_0^{\frac{\pi}{2}}\log(\xi(\alpha-\theta))F(\alpha-\theta)\cos(\hat{r}\xi(\alpha-\theta))\mathrm{d}\alpha + \int_0^{\pi} F(\alpha+\theta)\Im(\hat{r}\xi(\alpha+\theta))\mathrm{d}\alpha - \mathrm{i}\frac{\pi}{2}\int_0^{\pi} F(\alpha+\theta)\cos(\hat{r}\xi(\alpha+\theta))\mathrm{d}\alpha\right], \end{aligned} \tag{65}$$

where

$$F(\alpha) = \frac{4(\mu-\mu_*)\sin^2(\alpha)-\sigma}{\Lambda(\alpha)}\cos^2(\alpha). \tag{66}$$

For a point $\mathbf{y}$ at the boundary, Eq. (63) becomes

$$C^g_j v_j(\mathbf{y}) = \int_{\partial B}\tau_j(\mathbf{x})v^g_j(\mathbf{x},\mathbf{y})\mathrm{d}l_x - \int_{\partial B}\tau^g_j(\mathbf{x},\mathbf{y})v_j(\mathbf{x})\mathrm{d}l_x, \tag{67}$$

where C^g_j is the so-called $\mathbf{C}$-tensor [33], reducing to $\mathbf{I}/2$ for smooth boundaries and, more generally

$$C^g_i = \lim_{\varepsilon\to 0}\int_{\partial C_\varepsilon}\tau^g_i(\mathbf{x},\mathbf{y})\mathrm{d}l_x, \tag{68}$$

which coincides with the quasi-static value given in [5], since the 'dynamical terms' are non-singular, Eqs. (53).

Let us focus attention on a piecewise-rectilinear boundary (Fig. 2). Taking the source point $\mathbf{y}$ at the corner A, the boundary ∂B appearing in Eq. (67) can be split into the two portions FAB and BCDEF, so that Eq. (67) becomes

$$\begin{aligned} C^1_j v_j(\mathbf{y}) = &\underbrace{\int_{\partial B}\tau_j(\mathbf{x})v^1_j(\mathbf{x}-\mathbf{y})\mathrm{d}l_x}_{\text{weakly-singular}} - \underbrace{\int_{\mathrm{BCDEF}}\tau^1_j(\mathbf{x}-\mathbf{y})v_j(\mathbf{x})\mathrm{d}l_x}_{\text{non-singular}} - \underbrace{\int_{\mathrm{FAB}}\tau^1_{j\,\mathrm{dynamic}}(\mathbf{x}-\mathbf{y})v_j(\mathbf{x})\mathrm{d}l_x}_{\text{non-singular}} \\ &+T^1_2\underbrace{\int_{\mathrm{FA}}\frac{v_2(\mathbf{x})}{|\mathbf{x}-\mathbf{y}|}\mathrm{d}l_x}_{\text{strongly-singular}} - T^1_2\underbrace{\int_{\mathrm{AB}}\frac{v_2(\mathbf{x})}{|\mathbf{x}-\mathbf{y}|}\mathrm{d}l_x}_{\text{strongly-singular}} \end{aligned} \tag{69}$$

and

$$\begin{aligned} C^2_j v_j(\mathbf{y}) = &\underbrace{\int_{\partial B}\tau_j(\mathbf{x})v^2_j(\mathbf{x}-\mathbf{y})\mathrm{d}l_x}_{\text{weakly-singular}} - \underbrace{\int_{\mathrm{BCDEF}}\tau^2_j(\mathbf{x}-\mathbf{y})v_j(\mathbf{x})\mathrm{d}l_x}_{\text{non-singular}} - \underbrace{\int_{\mathrm{FAB}}\tau^2_{j\,\mathrm{dynamic}}(\mathbf{x}-\mathbf{y})v_j(\mathbf{x})\mathrm{d}l_x}_{\text{non-singular}} \\ &+T^2_1\underbrace{\int_{\mathrm{FA}}\frac{v_1(\mathbf{x})}{|\mathbf{x}-\mathbf{y}|}\mathrm{d}l_x}_{\text{strongly-singular}} - T^2_1\underbrace{\int_{\mathrm{AB}}\frac{v_1(\mathbf{x})}{|\mathbf{x}-\mathbf{y}|}\mathrm{d}l_x}_{\text{strongly-singular}}, \end{aligned} \tag{70}$$

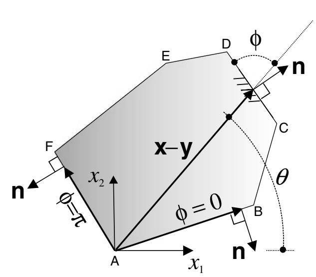

Fig. 2. Geometric representation of angles θ and ϕ for a polygonal domain. Note that ϕ is constant and equal to 0 (or π) when position vector $\mathbf{x}$–$\mathbf{y}$ is on the edge AB (or AF), while ϕ becomes a function of θ when $\mathbf{x}$–$\mathbf{y}$ is on the edge CD.

where T_2^1 and T_1^2 are the constants appearing in Eqs. (55)$_{3,4}$ for $\tau^1_{2\,\mathrm{static}}$ and $\tau^2_{1\,\mathrm{static}}$. The two strongly singular integrals in Eqs. (69) and (70) can be reduced to weakly singular integrals through integration by parts, thus obtaining

$$\int_{\mathrm{FA}} \frac{v_j(\mathbf{x})}{|\mathbf{x}-\mathbf{y}|}\mathrm{d}l_x - \int_{\mathrm{AB}} \frac{v_j(\mathbf{x})}{|\mathbf{x}-\mathbf{y}|}\mathrm{d}l_x = v_j(\mathrm{F})\log l_{\mathrm{FA}} - v_j(\mathrm{B})\log l_{\mathrm{AB}} - \int_0^{l_{\mathrm{FA}}} v_j'(r)\log r\,\mathrm{d}r + \int_0^{l_{\mathrm{AB}}} v_j'(r)\log r\,\mathrm{d}r, \tag{71}$$

where $v_j(\mathrm{F})$, $v_j(\mathrm{A})$ and $v_j(\mathrm{B})$ are the incremental displacements at corners F, A, B and prime denotes derivative with respect to a function's argument; l_{FA} and l_{AB} are the lengths of the edges FA and AB, respectively.

5.2. The discretization of the boundary and the collocation BEM

According to a boundary element formulation [11,31,48], the boundary ∂B is discretized into elements Γ^e, of length l_e, and, within each element, incremental displacement and traction are given the following representations

$$v_i = \varphi_\alpha(\xi)\bar{v}^e_{i\alpha}, \quad \dot{\tau}_i = \varphi_\alpha(\xi)\bar{\tau}^e_{i\alpha}, \quad \alpha = 0,\ldots,\Theta, \tag{72}$$

where $\xi \in [0,1]$, $\bar{v}^e_{i\alpha}$ and $\bar{\tau}^e_{i\alpha}$ are nodal incremental displacements and nominal tractions, respectively, φ_α are Lagrange polynomial shape functions of degree Θ, and repeated index α is to be summed between 0 and Θ. Using representation (72), the boundary integral Eqs. (69) and (70) can be written as

$$\begin{aligned} C_i^g v_i(\mathbf{y}^A) = {} & \sum_e \bar{\tau}^e_{i\alpha} l_e \int_0^1 \varphi_\alpha(\xi) v_i^g(\mathbf{x}(\xi),\mathbf{y}^{\mathrm{A}})\mathrm{d}\xi - \sum_{e\in\mathrm{BCDEF}} \bar{v}^e_{i\alpha} l_e \int_0^1 \varphi_\alpha(\xi)\tau_i^g(\mathbf{x}(\xi),\mathbf{y}^A)\mathrm{d}\xi - \sum_{e\in\mathrm{FAB}} \bar{v}^e_{i\alpha} l_e \\ & \times \int_0^1 \varphi_\alpha(\xi)\tau^g_{i\ \mathrm{dynamic}}(\mathbf{x}(\xi),\mathbf{y}^A)\mathrm{d}\xi + T_i^g\Bigg[v_i(\mathrm{F})\log l_{\mathrm{FA}} - v_i(\mathrm{B})\log l_{\mathrm{AB}} + \sum_{e\in AB} \bar{v}^e_{i\alpha}\int_0^1 \varphi_\alpha'(\xi)\log(r_e + l_e\xi)\mathrm{d}\xi \\ & - \sum_{e\in\mathrm{FA}} \bar{v}^e_{i\alpha}\int_0^1 \varphi_\alpha'(\xi)\log(r_e - l_e\xi)\mathrm{d}\xi\Bigg], \end{aligned} \tag{73}$$

where $T_1^1 = T_2^2 = 0$ and r_e indicates the distance from point $\mathbf{y}^A$ of the first edge node of the element, assuming element numbers increasing counterclockwise.

Integrals in Eq. (73) can be evaluated by standard Gauss quadrature rules. Moreover, also the weak singularity of the last two integrals in Eq. (73), involving the boundary elements containing the source node A, can be eluded by easy analytic integration. Following this way, for example in the particular case of linear shape functions,

$$\varphi_0(\xi) = 1-\xi, \quad \varphi_1(\xi) = \xi, \quad \varphi_\alpha'(\xi) = (-1)^{\alpha+1}, \quad \alpha = 0,1, \tag{74}$$

Eq. (73) takes the form

$$\begin{aligned} C_i^g v_i(\mathbf{y}^A) = {} & \sum_e \bar{\tau}^e_{i\alpha} l_e \int_0^1 \varphi_\alpha(\xi) v_i^g(\mathbf{x}(\xi),\mathbf{y}^{\mathrm{A}})\mathrm{d}\xi - \sum_{e\in\mathrm{BCDEF}} \bar{v}^e_{i\alpha} l_e \int_0^1 \varphi_\alpha(\xi)\tau_i^g(\mathbf{x}(\xi),\mathbf{y}^A)\mathrm{d}\xi - \sum_{e\in\mathrm{FAB}} \bar{v}^e_{i\alpha} l_e \\ & \times \int_0^1 \varphi_\alpha(\xi)\tau^g_{i\ \mathrm{dynamic}}(\mathbf{x}(\xi),\mathbf{y}^A)\mathrm{d}\xi + T_i^g\Bigg[v_i(\mathrm{F})\log l_{\mathrm{FA}} - v_i(\mathrm{B})\log l_{\mathrm{AB}} + \sum_{e\in\mathrm{B'B}} (-1)^{\alpha+1}\bar{v}^e_{i\alpha}\int_0^1 \log(r_e + l_e\xi)\mathrm{d}\xi \\ & - \sum_{e\in\mathrm{FF'}} (-1)^{\alpha+1}\bar{v}^e_{i\alpha}\int_0^1 \log(r_e - l_e\xi)\mathrm{d}\xi + (v_i(\mathrm{B'}) - v_i(\mathrm{A}))(\log l_{\mathrm{AB'}} - 1) - (v_i(\mathrm{A}) - v_i(\mathrm{F'}))(\log l_{\mathrm{F'}A} - 1)\Bigg], \end{aligned} \tag{75}$$

where $\mathrm{F'}$ and $\mathrm{B'}$ are the nodes next to source node A, on the left and right-hand side, respectively.

Collocating Eq. (75) at the boundary nodes yields an algebraic system which can be solved to obtain the unknown nodal values $\bar{v}^e_{i\alpha}$, $\bar{\tau}^e_{i\alpha}$ of incremental displacement and nominal traction on the portions of boundary where, correspondingly, incremental traction and displacement are prescribed.

6. Numerical examples highlighting the role of prestress

In all the following numerical examples, uniform meshes of rectilinear elements have been employed for boundary discretization. Linear shape functions have been adopted for incremental displacements and tractions at the boundary. Integrals involved in incremental displacements, relevant gradient and incremental pressure of the Green state, as well as integrals involved in the discretization of the boundary integral equations, have been evaluated by means of Gauss

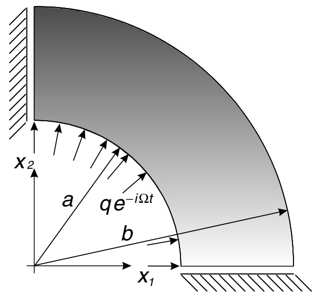

Fig. 3. Hollow elastic orthotropic cylinder, subject to time-harmonic pulsating internal pressure.

quadrature rules (a higher precision has been used for evaluation of the latter integrals)[4]. In all the examples, the axes of orthotropy and the principal directions of pre-stress coincide with the x_1 and x_2 axes.

6.1. Hollow cylinder subject to pulsating internal pressure

We start with the simple example of a hollow elastic, incompressible and orthotropic cylinder (taken infinitely long in the out-of-plane direction) subject to internal pressure, for which the analytical solution is known in the particular case of null pre-stress and isotropic constitutive law, see [40]. In particular (Fig. 3), the inner and outer radii of the shell are denoted by a and b, respectively, and the time-harmonic internal pressure is taken in the form

$$q(t) = q\mathrm{e}^{-\mathrm{i}\Omega t}. \tag{76}$$

The solution to this problem in the special case when $\mu = \mu_*$ and $k = 0$, depends on the radial distance r ($a \leqslant r \leqslant b$). A peculiarity of this problem is that the incompressibility constraint (for cylindrical coordinates under the assumption of radial symmetry) becomes

$$\frac{\partial u_r}{\partial r} + \frac{u_r}{r} = 0, \tag{77}$$

(where u_r is the radial component of displacement) which determines the displacement solution to be an integration constant times $1/r$, so that the equations of motion

$$\frac{\partial \sigma_r}{\partial r} + \frac{\sigma_r - \sigma_\theta}{r} = \rho \frac{\partial^2 u_r}{\partial t^2}, \tag{78}$$

(where σ_r and σ_θ are the radial and circumferential stresses) after substitution of the constitutive equations, immediately determine the in-plane hydrostatic pressure. The result is [40]

$$u_r = \frac{q}{2\mu m r}, \tag{79}$$

and

$$\begin{aligned} \sigma_r &= \frac{q}{m}\frac{r^2 - b^2}{r^2 b^2} + \frac{q\Omega^2}{2mc_0^2}\log\frac{b}{r}, \\ \sigma_\theta &= \frac{q}{m}\frac{r^2 + b^2}{r^2 b^2} + \frac{q\Omega^2}{2mc_0^2}\log\frac{b}{r}, \end{aligned} \tag{80}$$

where

$$m = \frac{b^2 - a^2}{a^2 b^2} + \frac{\Omega^2}{2c_0^2}\log\frac{a}{b}, \quad c_0 = \sqrt{\frac{\mu}{\rho}}. \tag{81}$$

[4] A general-purpose Fortran 90 code for two-dimensional incremental deformations superimposed upon a given uniform pre-strained state has been developed at the Solid & Structural Computational Mechanics Laboratory of the University of Trento, whose executable is available on: http://www.ing.unitn.it/dims/laboratories/comp_solids_structures.php.

Therefore, the solution depends on the dimensionless parameters

$$\frac{\Omega a}{c_0}, \quad \frac{a}{b}, \quad \frac{r}{b}, \quad \frac{q}{\mu}, \tag{82}$$

while, in the presence of anisotropy and pre-stress, the problem loses radial symmetry and additional parameters like μ/μ_* and $k = (\sigma_1 - \sigma_2)/(2\mu)$ are to be taken into account. It can be noted from Eqs. (79)–(80) that *there is only one natural frequency*[5], corresponding to $m = 0$, namely,

$$\frac{\Omega a}{c_0} = \sqrt{2\frac{1 - a^2/b^2}{\log(b/a)}}. \tag{83}$$

The geometry represented in Fig. 3 has been discretized employing 34 boundary elements of equal length and solved for $\mu_*/\mu = 1$ and $\mu_*/\mu = 1/2$. The Green tractions and the discretized boundary integral equation have been integrated employing 12 and 18 integration points, respectively. Results are reported in Fig. 4, in terms of the dimensionless quantities $2\mu u_r/(aq)$ (upper part), σ_r/q (central part), and σ_θ/q (lower part) versus $a\Omega/c_0$. In the isotropic case, the numerical solution is compared with the analytical solution (79)–(80), showing a fairly good agreement. All the quantities have been plotted at the point $r = (a + b)/2$ and for $b/a = 2$. Plotting of the stress fields has implied the use of the boundary equation for the pressure increment (64). Note that in the anisotropic case, two natural frequencies appear, showing that anisotropy of material changes the dynamic behaviour completely with respect to the isotropic case.

6.2. A circular hole with pulsating internal tractions in an infinite elastic medium

To highlight that the boundary element method is particularly suitable for analyzing steady-state vibration of infinite media (since the radiation condition is automatically taken into account), a circular hole (Fig. 5) is considered, in an orthotropic infinite elastic medium, symmetrically loaded by a time-harmonic pulsating pressure (76) on two portions of the boundary (each one has an angulare amplitude of 20°). The circular cavity has been discretized by employing a uniform mesh of 64 elements with 24 Gauss points for the integration of Green's functions for applied tractions and 36 Gauss points for the evaluation of boundary integrals. The real and imaginary parts of radial displacement at the mid point of the loaded cavity sector (non-dimensionalized by the coefficient μ/qa) is reported as a function of the dimensionless frequency $\Omega a/c_0$ for isotropic $\mu_*/\mu = 1$ and anisotropic $\mu_*/\mu = 1/2$ elasticity in Fig. 6 upper part and lower part, respectively.

The fact that the solution involves a real and imaginary part is a consequence of the fulfillment of the radiation condition at infinity. The shapes of the cavity are plotted in Fig. 7, taking the real and the imaginary components of displacement separately at different values of $\Omega a/c_0 = \{0.5, 1, 2, 3, 4\}$. Only the isotropic case is reported for the sake of brevity.

6.3. Elastic block under pulsating lateral nominal tractions

The same geometries considered for quasi-static loading in [12] is now considered for time-harmonic antisymmetric and symmetric normal, incremental dead-loading. The two analyzed problems are sketched in Fig. 8, where a rectangular block, made up of Mooney–Rivlin elastic material, is subject to a vertical, compressive pre-stress, transmitted by two smooth, rigid constraints and loaded on two portions (1/9 of the edge length) of the otherwise free lateral edges. For both cases, uniform meshes of 72 boundary elements have been employed, with 24 and 36 Gauss points for integration of Green's function and boundary elements, respectively.

Results for the antisymmetric and symmetric loading geometries shown in Fig. 8 are reported in Fig. 9 on the left and on the right, respectively. In particular, the horizontal displacement u_1 normalized through multiplication by $\mu/(b\tau)$ of points with label 'E' in Fig. 8 is reported versus the dimensionless frequency $\Omega b/c_0$, where $c_0 = \sqrt{\mu/\rho}$ is the propagation speed of a wave in the isotropic material at null pre-stress. The upper parts of the figure refer to null pre-stress, $k = 0$, while the central parts to $k = 0.4$ and the lower parts to $k = 0.52$ ($k = 0.8$) for the antisymmetric, shown on the left, (symmetric, shown on the right), loading. The last values are close to the bifurcation values under quasi-static load, respectively, $k = 0.522$ and $k = 0.839$, the former value corresponding to an antisymmetric bifurcation and the latter to a symmetric surface mode of null wavelength. Comparison is made with results obtained by using ABAQUS-Standard (Ver. 6.2-Hibbitt, Karlsson & Sorensen Inc.), with plane-strain, 4-nodes bilinear, hybrid elements (CPE4H), and a total number of 1296 finite elements.

The figure clearly shows the natural frequencies of the system, which are also reported in Table 1 in the case of antisymmetric loading. Figure and table highlight that the natural frequencies of the system get lower and lower for increasing

[5] The fact that there is only one natural frequency may seem erroneous at a first glance, but can be justified by the fact that radial symmetry and incompressibility produce a system which possesses only one degree of freedom, in the sense that a radial displacement of the inner surface of the cylinder directly determines the displacement at every points.

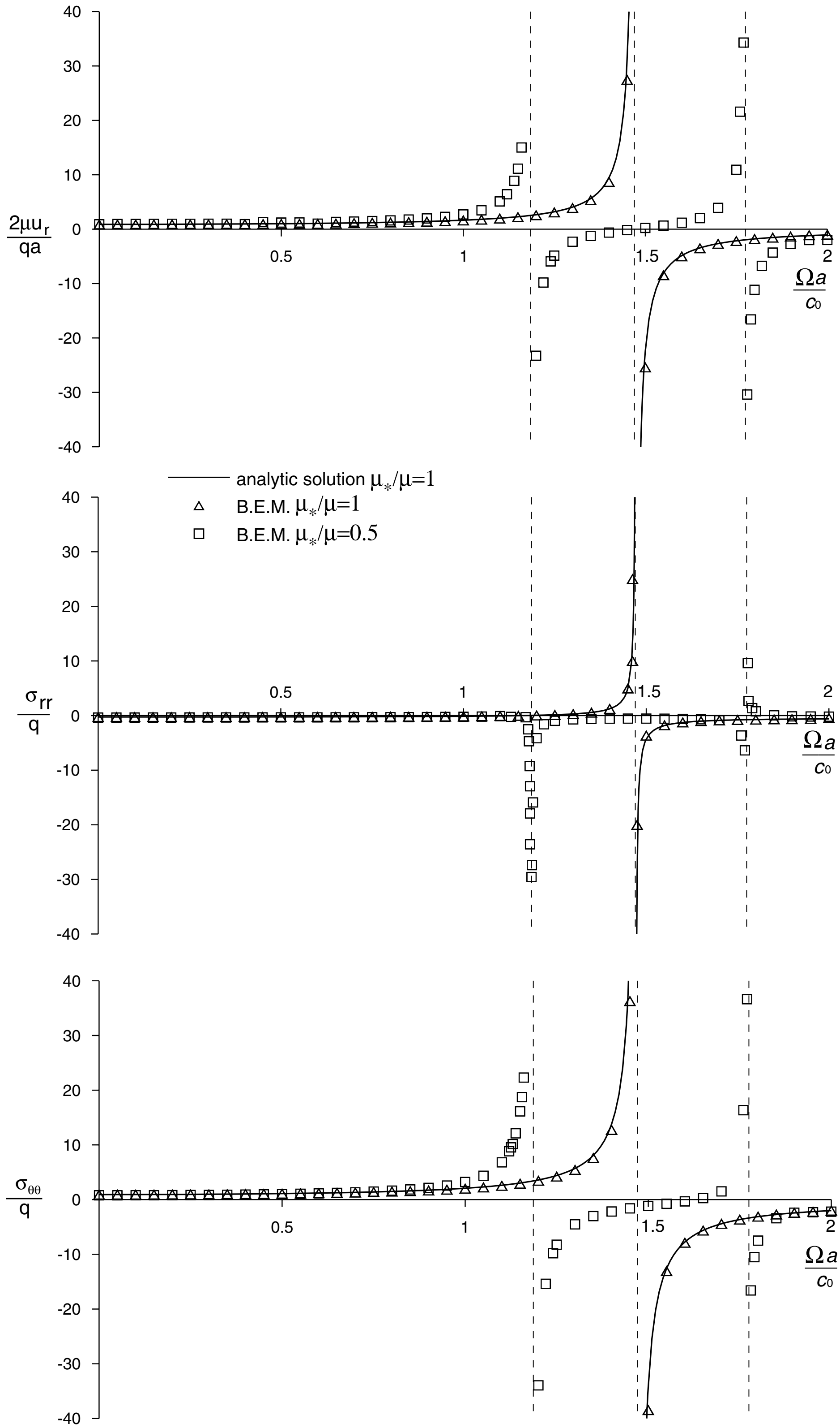

Fig. 4. Dimensionless radial displacement (upper part), radial stress (central part) and circumferential stress (lower part) at $r = (a + b)/2$ for the problem sketched in Fig. 3 (with $b = 2a$), versus dimensionless frequency $\Omega a/c_0$, for anisotropic $\mu_*/\mu = 1/2$ and isotropic $\mu_*/\mu = 1$, incompressible elasticity. Two natural frequencies are shown for the anisotropic case, while only one exists for isotropic behaviour.

pre-stress levels, according to the fact that all natural frequencies will migrate towards zero when the pre-stress corresponding to the quasi-static bifurcation will be approached. Note also that there is a loss of precision of the results obtained with ABAQUS for symmetric loading.

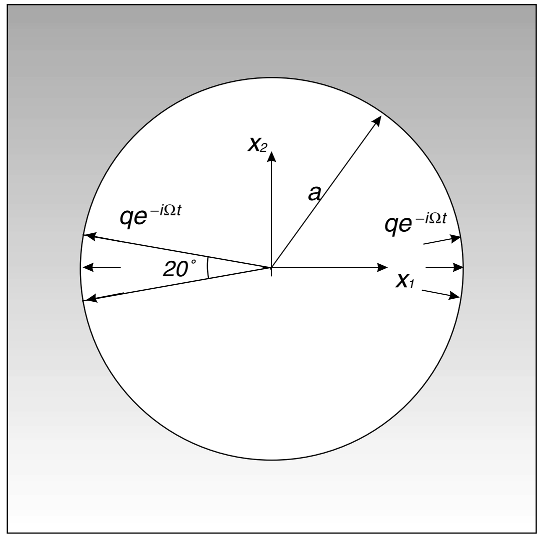

Fig. 5. Infinite, orthotropic elastic medium with a circular hole symmetrically loaded on two portions of the boundary by a time-harmonic pulsating pressure. The angular amplitude of each loaded sector is 20°.

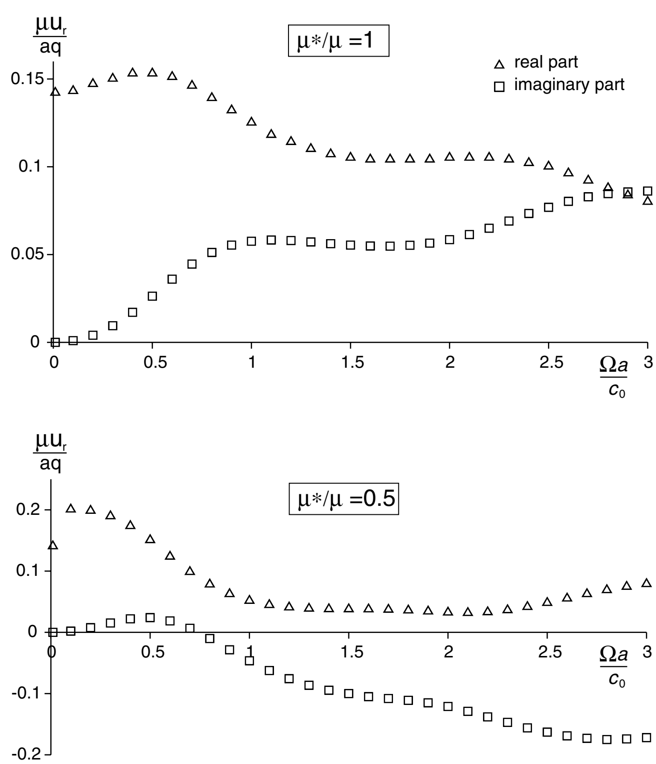

Fig. 6. Real and imaginary parts of the radial displacement (multiplied by μ/qa) at the mid point ($x_1 = a$, $x_2 = 0$) of the loaded portion of the hole (see Fig. 5), versus dimensionless frequency $\Omega a/c_0$. Upper part: isotropic, incompressible elasticity with $\mu_*/\mu = 1$; lower part: anisotropic, incompressible elasticity with $\mu_*/\mu = 1/2$.

The in-plane hydrostatic stress increment, evaluated with the boundary integral Eq. (64) is plotted in Fig. 10 at points labelled A, B, C, and D in Fig. 8 (with spatial coordinates $x_1/b = \{-0.5, 0.5\}$ and $x_2/b = \{-0.5, 0.5\}$), for a pre-stress $k = 0.4$. Different values of dimensionless frequency have been considered, namely, $\Omega b/c_0 = \{0.5, 1.5, 2\}$. Antisymmetric loading is reported in the upper part of the figure, while symmetric loading in the lower. The comparison with ABAQUS reported in Fig. 10, represents the first numerical validation of the boundary integral equation obtained by Bigoni and Capuani [6] for in-plane pressure increments in the dynamic range.

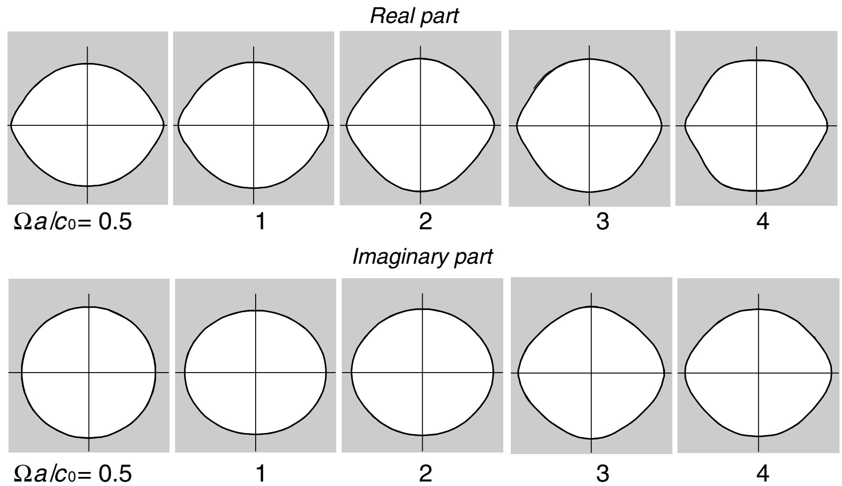

Fig. 7. Shapes of the circular hole (see Fig. 5) for isotropic $\mu_*/\mu = 1$ elasticity. Real (upper figure) and imaginary (lower figure) parts of displacement are reported at different values of $\Omega a/c_0$.

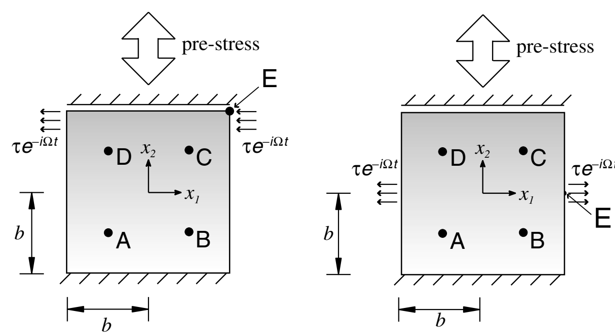

Fig. 8. Elastic, incompressible orthotropic block subject to time-harmonic antisymmetric (left) and symmetric (right) perturbation.

6.4. Shear bands for dynamic loading

6.4.1. Analytic solution of an example of Ryzhak boundary conditions: elastic block under pure shear deformation

A rectangular, incompressible and orthotropic elastic block (of dimensions $b \times h$) is considered, subjected to a pre-stress whose principal directions are aligned parallel to the edges of the block as well as to the orthotropy axes.

The boundary conditions are (Fig. 11):

- null horizontal incremental tractions and vertical incremental displacement:

$$\dot{t}_{11} = 0, \quad v_2 = 0, \tag{84}$$

  along the vertical edges at $x_1 = 0$ and $x_1 = b$;
- null displacements:

$$v_1 = 0, \quad v_2 = 0, \tag{85}$$

  along the horizontal edge at $x_2 = 0$;
- prescribed time-harmonic shear tractions and null vertical displacement:

$$\dot{t}_{21} = \tau e^{-i\Omega t}, \quad v_2 = 0, \tag{86}$$

  along the horizontal edge at $x_2 = h$.

The boundary conditions, the type of orthotropy and the geometric setting correspond to a case belonging to the class of boundary value problems analyzed by Ryzhak [44,45] and for which uniqueness and stability have been proved, under quasi-static incremental loading and the strong ellipticity assumption (see, e.g. [12]). Strong ellipticity, under the assumption $\mu > 0$ (holding here and in [5,6,11,12]), coincides with the ellpiticity condition $\Lambda(\alpha) > 0$, Eq. (19).

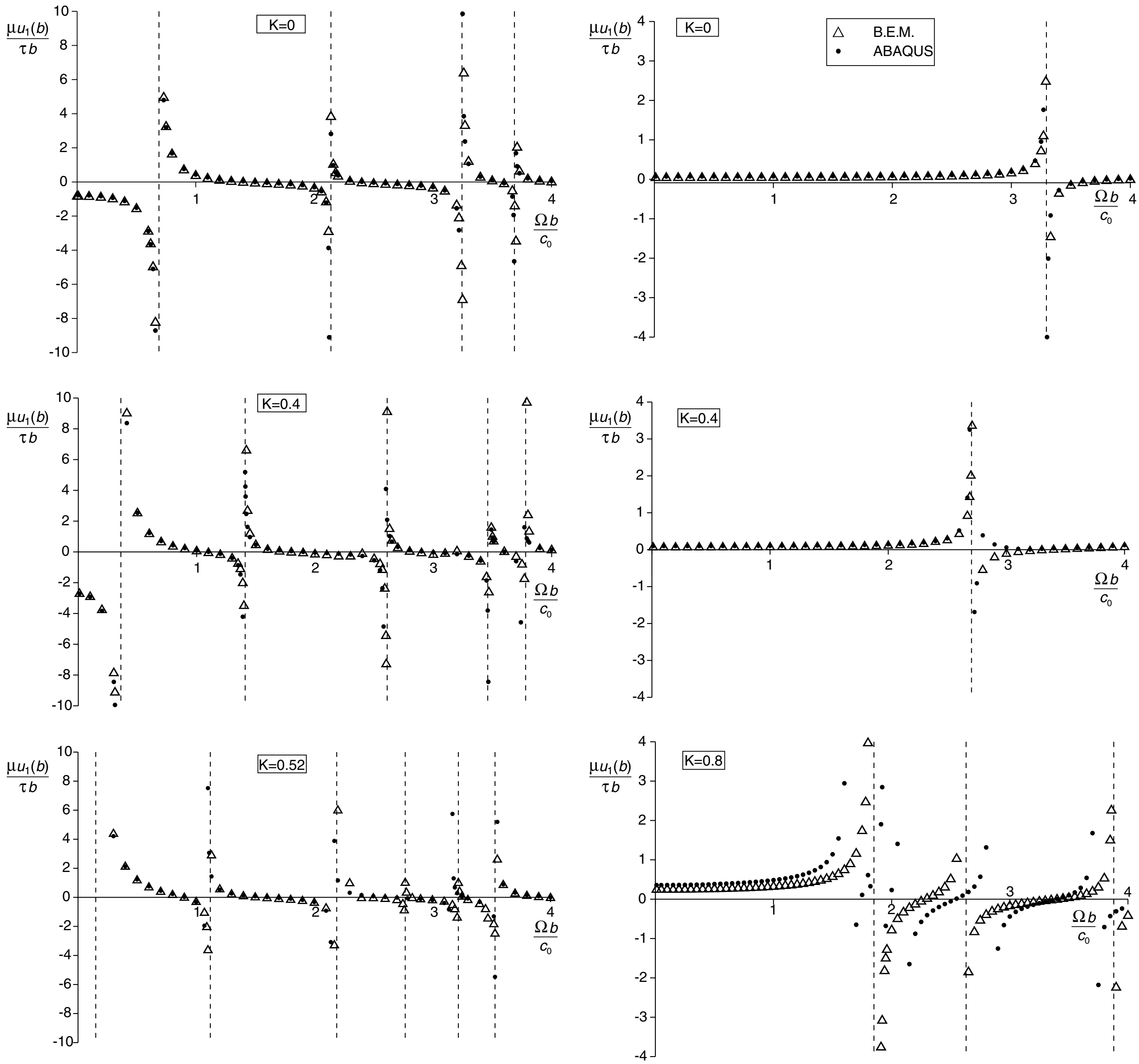

Fig. 9. Horizontal displacement $\mu u_1/(b\tau)$ of point E in Fig. 8, versus dimensionless frequency $\Omega b/c_0$ at null pre-stress (upper part), at high, compressive pre-stress, $k = 0.4$ (central part), and at a compressive pre-stress, $k = 0.52$ (left) and $k = 0.8$ (right), close to a quasi-static bifurcation (lower part). Antisymmetric loading is reported on the left, while symmetric loading on the right.

Table 1
The lowest six dimensionless natural frequencies $\Omega b/c_0$ for the elastic block of Fig. 8 (left) subject to antisymmetric lateral load, at different compressive pre-stress levels k

k	$\Omega b/c_0$					
0	0.69	2.14	3.25	3.71	4.73	5.26
0.4	0.36	1.41	2.61	3.46	3.78	4.60
0.52	0.15	1.12	2.19	2.77	3.22	3.53

Taking the nominal incremental stress field

$$\dot{t}_{11} = \dot{t}_{22} = 0, \quad \dot{t}_{21} = \mu(1-k)v_{1,2}, \quad \dot{t}_{12} = (\mu - p)v_{1,2}, \tag{87}$$

assuming a solution in the form

$$v_1(x_1, x_2) = \bar{v}_1(x_2)\mathrm{e}^{-\mathrm{i}\Omega t}, v_2(x_1, x_2) = 0, \quad \dot{\pi}(x_1, x_2) = 0 \tag{88}$$

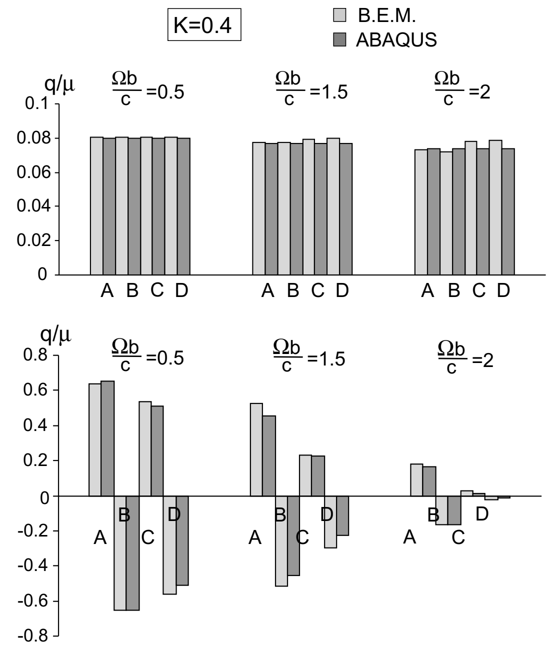

Fig. 10. Internal in-plane hydrostatic stress increment q/μ at points A, B, C, D in Fig. 8, for a compressive pre-stress $k = 0.4$.

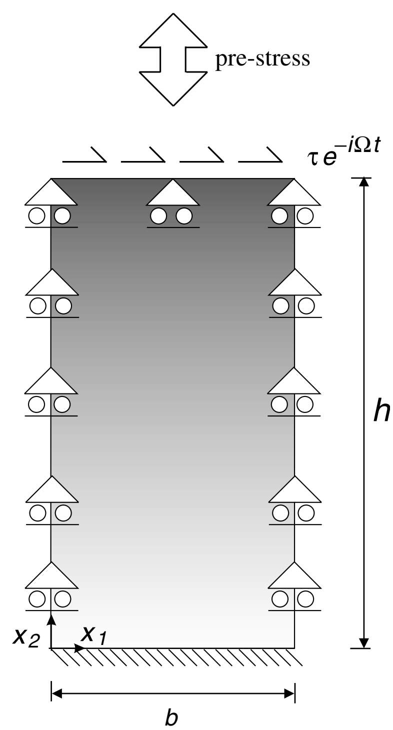

Fig. 11. Incompressible, orthotropic elastic block with boundary conditions of the type investigated by Ryzhak, subjected to time-harmonic nominal shear stresses.

and substituting in the equations of motion (7), with null incremental body forces $\dot{f}_j = 0$, leads to the non-trivial equation

$$\frac{\mathrm{d}^2\bar{v}_1}{\mathrm{d}x_2^2} = -\frac{\Omega^2}{c_L^2}\bar{v}_1, \tag{89}$$

where

$$c_L = \sqrt{\frac{\mu(1-k)}{\rho}}, \tag{90}$$

is the propagation velocity of a transverse plane wave travelling parallel to x_2-axis.

By solving the differential Eq. (89) and imposing the boundary conditions $(85)_1$ and $(86)_1$, we obtain

$$v_1(x_2,t) = \frac{\tau}{\Omega\sqrt{\rho\mu(1-k)}}\left[\cos\left(\frac{\Omega h}{c_L}\right)\right]^{-1}\sin\left(\frac{\Omega x_2}{c_L}\right)\mathrm{e}^{-\mathrm{i}\Omega t}, \tag{91}$$

representing the solution to our problem.

Note that the limit for $\Omega \to 0$ gives the quasi-static solution

$$v_1(x_2) = \frac{x_2\tau}{\mu(1-k)}, \tag{92}$$

and that the eigenfrequencies are given by

$$\Omega = \frac{n\pi}{2}\frac{c_L}{h}, \quad n = 1,3,5\ldots. \tag{93}$$

Note that both the time-harmonic and the quasi-static solutions, Eqs. (91) and (92), do not involve the material parameter μ_*. These solutions are therefore valid for every value of $\mu \neq 0$ and $k \neq 1$ (although for $\mu(1-k) < 0$ the horizontal displacement results opposite to the applied shear loading), so that they hold true also beyond failure of ellipticity, occurring when $\Lambda(\alpha) = 0$, for at least one α. This circumstance should not surprise, in the sense that a solution to a boundary value problem may exist even beyond stability (as for instance in the case of the trivial solution in the Euler beam buckling, still existing beyond the first buckling load). In the limit $k \to 1$, the material becomes vanishing stiff in the horizontal direction (so that the corresponding displacement becomes infinite), so that at $k = 1$ a horizontal strain-discontinuity shear band becomes possible. It should also noted that the eigenfrequencies tend to zero, when the shear wave velocity c_L vanishes.

It can be observed from Eq. (91) that the value $\mu(1-k)v_1(h)/(\tau h)$ depends only on $\Omega h/c_L$ and this feature is exploited to evaluate the numerical performance of our approach. To this purpose, the geometry reported in Fig. 11 has been discretized employing a uniform mesh of 72 boundary elements. Here the number of Gauss points used for the integrations has been increased with increasing pre-stress levels, since the numerical accuracy tends to diminish when the pre-stress approaches the boundary of the elliptic region. In particular, 12 and 18 Gauss points (the former number refers to integrals of Green's function and the latter to integrals over boundary elements) have been employed for $k = 0$; 24 and 36 Gauss points for $k = 0.4$; 48 and 72 Gauss points for $k = 0.9$.

Results in terms of the horizontal displacement [multiplied by $\mu(1-k)/(\tau h)$] at $x_2 = h$ versus $\Omega h/c_L$ are reported in Fig. 12. Three different values of pre-stress $k = \{0, 0.4, 0.9\}$ have been considered in the figure to test our numerical procedure (although the analytical solution reported in the figure has been made independent of k), approaching the loss of ellipticity, which occurs at $k = 1$ for Mooney–Rivlin material. It can be concluded from the figure that the numerical pro-

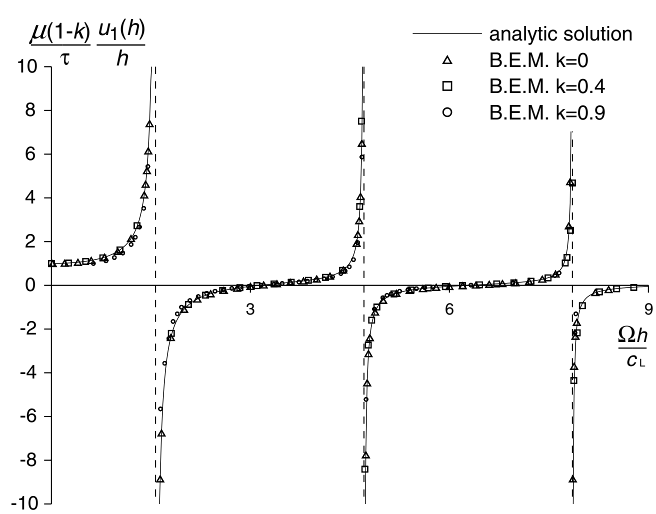

Fig. 12. Dimensionless horizontal displacement at $x_2 = h$ for an elastic anisotropic block subject to time-harmonic pulsating shear (see Fig. 11) versus dimensionless frequency $\Omega h/c_L$. Different pre-stress levels k have been considered to check the accuracy of the method.

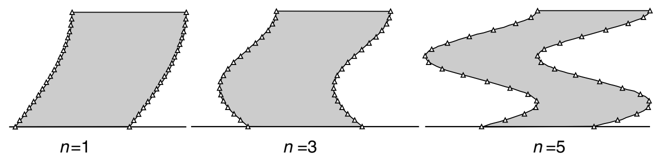

Fig. 13. The first three natural vibration modes evaluated numerically and superimposed to the analytic solution for the elastic block shown in Fig. 11.

cedure is quite accurate, but the precision decreases for increasing k, so that the number of Gauss points has to be increased to get results with comparable accuracy.

The first three natural vibration modes have been numerically obtained and are superimposed for comparison to the analytical solution in Fig. 13. Beside the fair agreement between numerical and analytical results, we may note that the vibrational modes [as well as every deformation solution of Eq. (91)] consist of a pure shear deformation, so that the elastic block deforms similarly to a deck of cards.

6.5. Shear bands induced by perturbations

The boundary value problem presented in the previous section allows the approach of the elliptic boundary without prior 'encountering' bifurcation or instability thresholds. However, due to the absence of any perturbation, the incremental displacement fields (not reported for conciseness) do not evidence any kind of strain concentration into deformation bands. To highlight the possibility of such focussing of deformation, we analyze the boundary value problem sketched in Fig. 14 on the left for Mooney–Rivlin material $\mu_*/\mu = 1$, and on the right for an anisotropic material with $\mu_*/\mu = 1/4$. Both these boundary value problems are examples of Ryzhak boundary conditions. In particular, in Fig. 14 on the left, null displacements are prescribed on the whole boundary, except for two symmetric regions along the vertical edges (of length $c/b = 3/10$), where vertical displacements are null, but horizontal, uniform time-harmonic tractions are prescribed. Displacements are also null on the whole boundary in Fig. 14 on the right, except for a region of length c on the left edge and two regions of length $c/2$ near the corners of the right edge, where horizontal, uniform time-harmonic tractions are prescribed.

Results are presented in Figs. 15 and 16 where the level sets of the modulus of incremental displacements are reported for $\mu_*/\mu = 1$ and $\mu_*/\mu = 1/4$, and different values of pre-stress k.

Two values of dimensionless frequency parameter $\Omega b/c_0 = \{0.001, 4.3\}$ are investigated both for Mooney–Rivlin and for $\mu_*/\mu = 1/4$. The value of frequency $\Omega b/c_0 = 0.001$ is so low that the response is nearly quasi-static. We may note from Fig. 15 that the employed boundary conditions tend to focus the deformation along the horizontal axis, but this focussing becomes dramatic when the elliptic boundary is approached, $k = 0.88$. In particular, loss of ellipticity for a Mooney–Rivlin material occurs at $k = 1$, corresponding to an infinite stretch (see [6] for details). It is therefore usually believed that for such material shear bands are not possible, and this is in fact true if shear bands are intended as the emergence of strain-rate discontinuities. However, as pointed out by Bigoni and Capuani [5,6], shear bands, intended as a deformation concentration, become visible using a perturbative approach still within the elliptic range. Such a concentration of deformation is clearly visible in Fig. 15 for $k = 0.88$. Moreover, for high frequency ($\Omega b/c_0 = 4.3$), the deformation pattern degenerates into nearly horizontal plane parallel waves. Due to the fact that the modulus of incremental displacements is plotted, the spacing between these plane waves is one half of the corresponding wavelength.

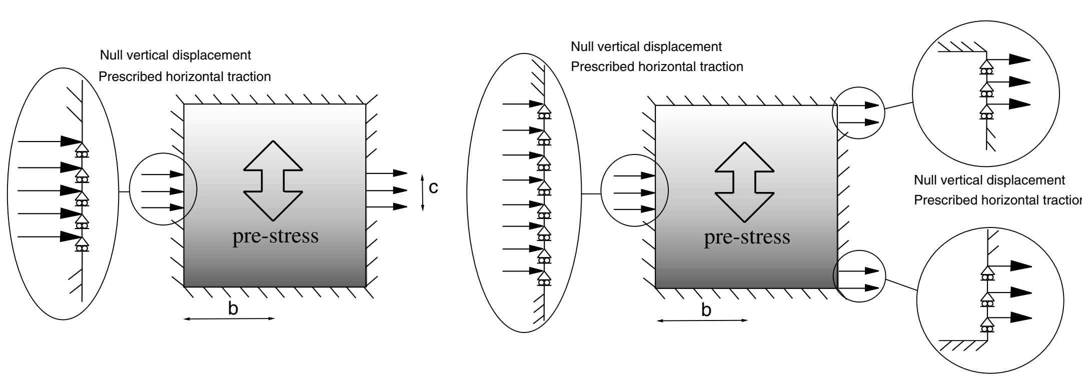

Fig. 14. Time-harmonic loading of an elastic block under boundary conditions investigated by Ryzhak. Left: null prescribed displacement on the whole boundary, except for the two zones of length c, where vertical displacements are null and horizontal loading is prescribed. Right: null prescribed displacement on the whole boundary, except for one zone of length c on the left edge and two zones of length $c/2$ near the corners of the right edge, where vertical displacements are null and horizontal loading is prescribed.

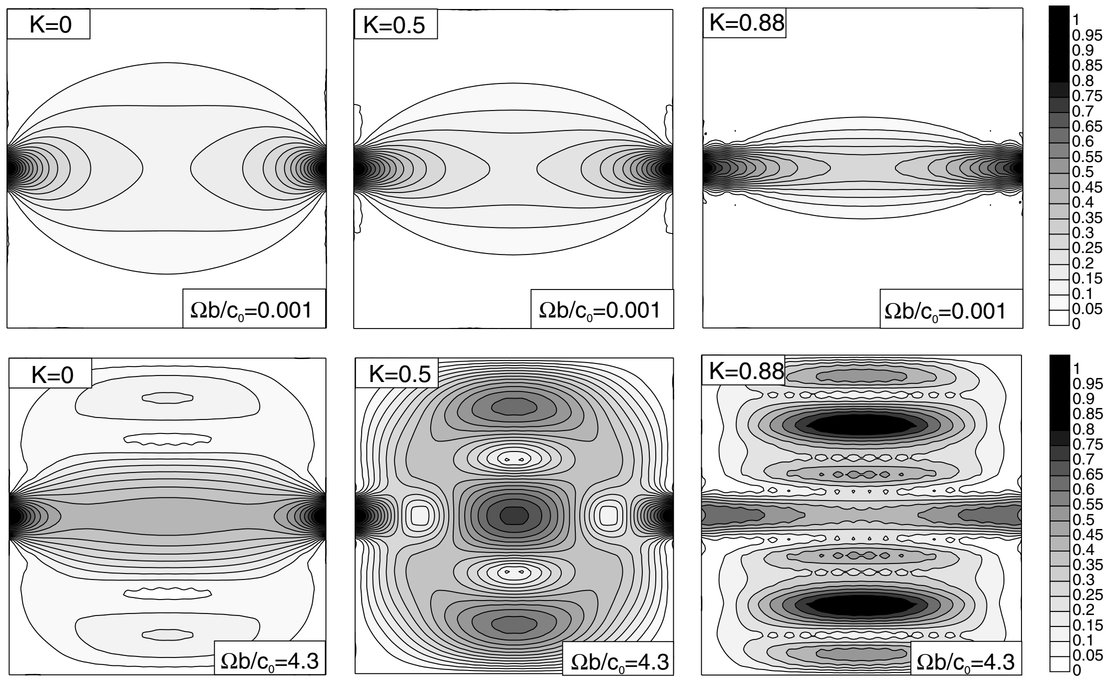

Fig. 15. Level sets of the modulus of incremental displacements for the boundary value problem sketched in Fig. 14 on the left. A Mooney–Rivlin material, $\mu_*/\mu = 1$, is considered at different values of pre-stress k and dimensionless frequency parameter $\Omega b/c_0$. In particular, $\Omega b/c_0 = 0.001$ corresponds to a quasi-static approximation. Note the emergence of shear bands for $k = 0.88$, i.e. when the elliptic boundary is approached.

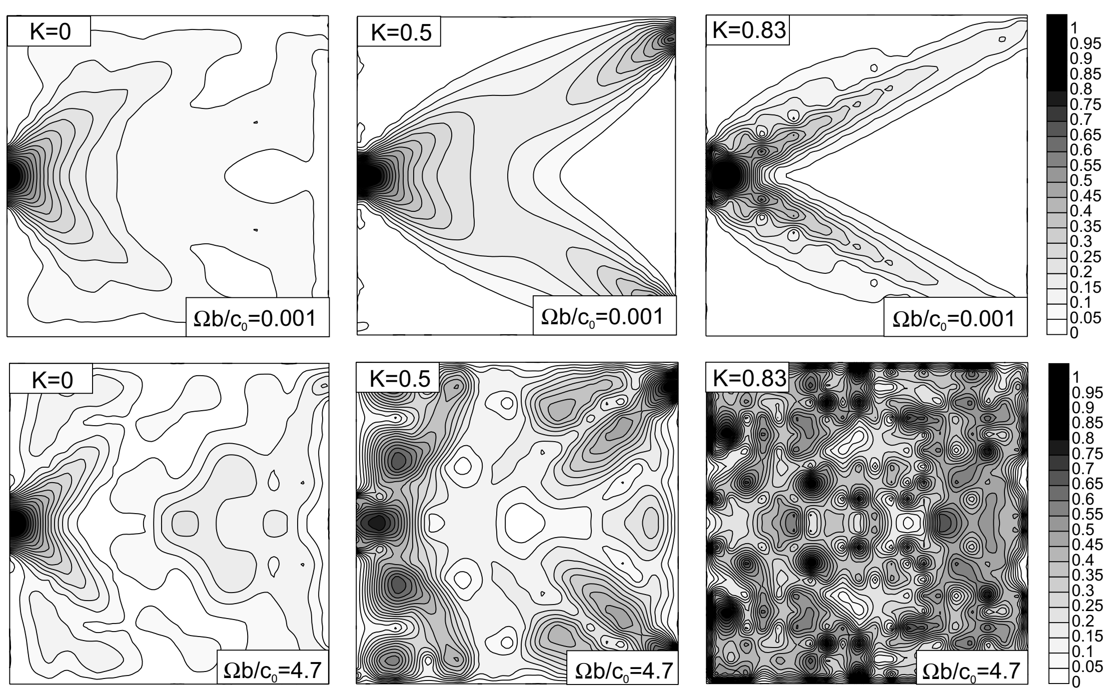

Fig. 16. Level sets of the modulus of incremental displacements for the boundary value problem sketched in Fig. 14 on the right. An anisotropic material, $\mu_*/\mu = 1/4$, is considered at different values of pre-stress k and dimensionless frequency parameter $\Omega b/c_0$. In particular, $\Omega b/c_0 = 0.001$ corresponds to a quasi-static approximation; in this case, note the clear emergence of shear bands for $k = 0.83$, i.e. when the elliptic boundary is approached.

For $\mu_*/\mu = 1/4$, loss of ellipticity occurs at $k \approx 0.866$, so that we may see that approaching this value ($k = 0.83$ in the figure), shear bands becomes visible in Fig. 16 at low frequency, $\Omega b/c_0 = 0.001$, while wave interactions tend to modify the structure of the shear bands into a complex pattern at high frequency, $\Omega b/c_0 = 4.3$.

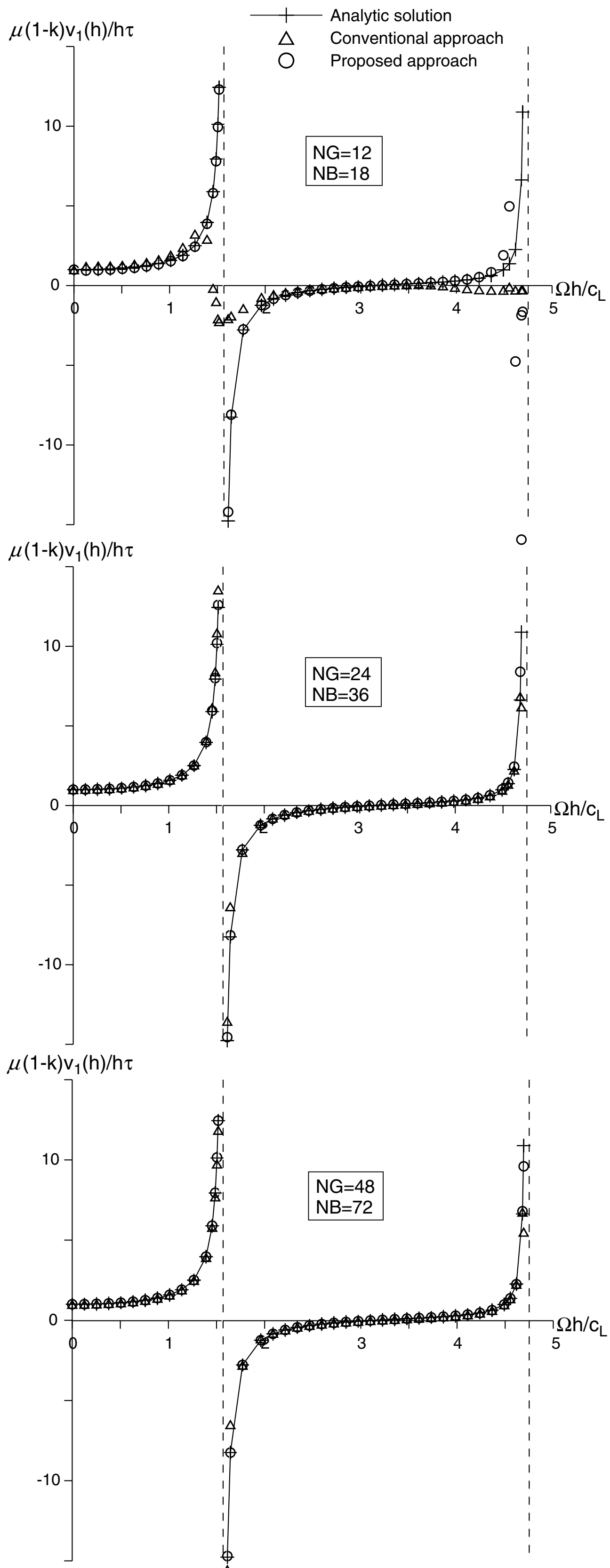

Fig. 17. Performance comparison between the proposed approach based on the directly-derived traction Green's function, Eqs. (53) and (55), and the conventional approach' based on the traction obtained from the displacement Green's function. The problem with Ryzhak boundary conditions (Figs. 11 and 12) is analyzed. The accuracy corresponding to increasing numbers of integration Gauss points for Green functions (NG) and boundary elements (NB) is shown in comparison with the analytical solution.

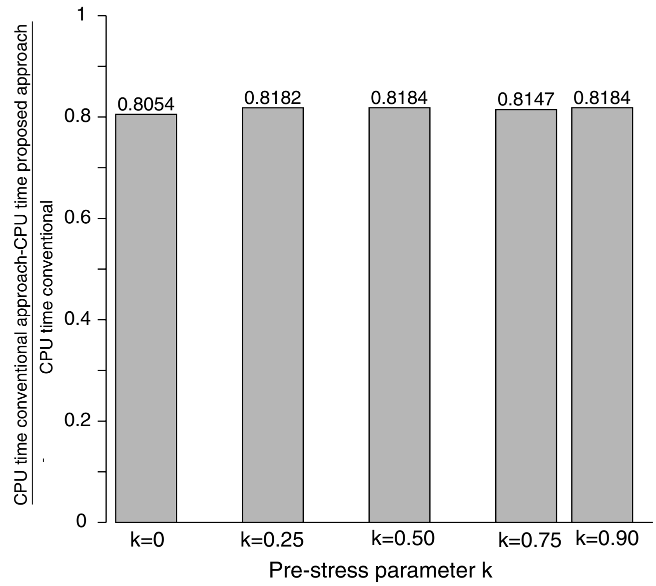

Fig. 18. Performance comparison between the proposed approach based on the directly-derived traction Green's function, Eqs. (53) and (55), and the 'conventional approach' based on the traction obtained from the displacement Green's function. The problem with Ryzhak boundary conditions (Figs. 11 and 12) is analyzed. CPU times are analyzed for different values of pre-stress k.

We remark finally that the above simple examples show how the perturbation technique introduced by Bigoni and Capuani [5,6] can be used to visualize the complex wave patterns emerging in proximity of the elliptic boundary.

7. The numerical performance of the proposed approach

A novel formula for the Green's function for incremental tractions has been derived, Eqs. (53) and (55). This formula is much simpler and direct than that usually obtained taking the gradient of the Green's function for incremental displacements and applying the constitutive tensor. We therefore expect that a boundary element technique based on the former formula is much more efficient than one based on the latter. To quantify the advantage of the novel technique, comparing computing times and precision, we have implemented both formulae in our boundary element computer code.

We have analyzed several cases and found comparable results, so that, for the sake of conciseness, we report in Fig. 17 results only for the boundary value problem analyzed in Section 6.4.1 (see Figs. 11 and 12), for which the analytical solution is known. The three graphs in Fig. 17 are similar to the graph presented in Fig. 12, but here they show the numerical solution corresponding to different number of Gauss points for integration of the Green's functions (label 'NG'), and for the spatial integration over the boundary elements (label 'NB'). Both the numerical results given by the alternative formulations of the fundamental solution are reported. In particular, the approach based on the Green's function given by Eqs. (53) and (55) is labelled 'Proposed approach', while the other 'Conventional approach'. We can see that the proposed approach is characterized by a higher precision near the resonance vibration frequencies, and the conventional approach shows a significant loss of accuracy at low values of Gauss points, NG and NB.

A comparison between the CPU times obtained using the two approaches is reported in Fig. 18, where the CPU time measured employing the proposed approach, subtracted to the time measured using the conventional approach (and the result normalized through division by the latter time), is reported as a function of the pre-stress k. Although the solution reported in Fig. 17 is not affected by k, this parameter enters the numerical procedure, which becomes heavier when k approaches the limit of ellipticity ($k = 1$). It is evident from Fig. 18 that the proposed approach yields a great reduction in the CPU times (only weakly dependent on k), thus confirming its superior efficiency.

8. Conclusions

We have introduced a boundary element formulation for time-harmonic, small-amplitude vibrations, superimposed upon a homogeneous plane strain deformation of an orthotropic, incompressible solid. A new expression for the Green's function for incremental applied tractions has been obtained (Eqs. (53) and (55)), which turns out to be particularly suitable for numerical calculations. In particular, our results reveal that the use of the new expression yields both a huge increase in performance and an excellent gain in precision, when compared to the usual procedure in which the employed

Green's function for incremental applied tractions is obtained from the gradient of the Green's function for incremental displacements.

The proposed boundary element technique has proved to be suitable to analyze time-harmonic, small-amplitude vibrations superimposed upon homogeneously pre-stressed, incompressible elastic solids. The main advantages of the method are as follows:

- the treatment of the incompressibility constraint does not cause any problem;
- in the case of inclusions in infinite domains, the technique allows automatic consideration of the radiation condition at infinity and is especially convenient, since only the boundary of the inclusion is discretized;
- the technique can be used to analyze, with satisfying accuracy, localized deformation patterns emerging near the boundary of loss of ellipticity;
- The proposed approach, based on the explicit expression of the incremental-traction fundamental solution, Eqs. (53) and (55), is much more efficient than the conventional approach (employed for instance by Brun et al. [11] for quasi-static loading).

Another important feature of our boundary element technique is that it allows investigation of vibrational properties of structures loaded near bifurcation points or shear bands thresholds. Therefore, the technique represents the 'dynamical counterpart' of the approach presented by Brun et al. [11,12] and allows investigation of features of instability not directly approachable through conventional techniques.

As a final comment, we remark that the pre-stress has been shown to strongly influence the vibrational response of structures, so that the presented numerical technique may become a useful tool for analyzing the behaviour of highly pre-stressed mechanical systems.

Acknowledgements

Financial support of MURST-Cofin 2005, prot. 2005085973_002 (D.B. and S.C.) and of MIUR-PRIN 2005 prot. 2005085158_001 (D.C.) is gratefully acknowledged.

Appendix A. On the singular integrals in Eqs. $(51)_{1,2}$

We consider now Eq. $(51)_1$ and begin by noting that

$$\oint_{|\boldsymbol{\omega}|=1} \frac{n_1}{\omega_1} \frac{d\omega}{\boldsymbol{\omega}\cdot\mathbf{x}} = \frac{n_1}{r}\int_0^{2\pi} \frac{d\alpha}{\cos\alpha\cos(\alpha+\theta)} = 0, \tag{A.1}$$

so that, assuming (52), Eq. $(51)_1$ can be written as

$$\tau^1_{1\,\mathrm{static}} = \frac{1}{2\pi^2(1+k)r}\int_0^{\pi}[(1-k)\tan(\alpha+\theta)-(2-k-\chi)\sin(\alpha+\theta)\cos(\alpha+\theta)]\frac{\cos\phi\cos\alpha+\sin\phi\sin\alpha}{\cos\alpha\Lambda(\alpha+\theta)}d\alpha. \tag{A.2}$$

Since the factor multiplying $\cos\phi$ vanishes in Eq. (A.2), we get the form $(54)_1$ of quasi-static traction.

Let us consider now Eq. $(51)_2$ and note that

$$\oint_{|\boldsymbol{\omega}|=1} \frac{n_2}{\omega_2} \frac{d\omega}{\boldsymbol{\omega}\cdot\mathbf{x}} = \frac{n_2}{r}\int_0^{2\pi} \frac{d\alpha}{\cos\alpha\sin(\alpha+\theta)} = 0, \tag{A.3}$$

so that we can write

$$\tau^2_{2\,\mathrm{static}} = -\frac{1}{2\pi^2(1+k)r}\int_0^{\pi}[(1+k)\cot(\alpha+\theta)-(2+k-\chi)\sin(\alpha+\theta)\cos(\alpha+\theta)]\frac{\cos\phi\cos\alpha+\sin\phi\sin\alpha}{\cos\alpha\Lambda(\alpha+\theta)}d\alpha. \tag{A.4}$$

Since the factor multiplying $\cos\phi$ vanishes in Eq. (A.4), we get the form $(54)_2$ of quasi-static traction.

Appendix B. Regularization of the quasi-static tractions $(54)_{1,2}$

The regularized expressions (55) have been derived by using the following Cauchy principal values

$$\int_0^{\pi}\frac{d\alpha}{\pi/2-\alpha} = 0, \quad \int_0^{\pi}\frac{d\alpha}{\beta-\alpha} = \log\left|\frac{\beta}{\beta-\pi}\right|. \tag{B.1}$$

Regularized equations alternative to (55) can be obtained, assuming $0 \leqslant |\theta| \leqslant \pi$ and using the Cauchy principal values

$$\int_0^{\pi} \frac{d\alpha}{\cos\alpha} = 0, \tag{B.2}$$

$$\int_0^{\pi} \frac{d\alpha}{\cos(\alpha+\theta)} = \begin{cases} -4\tanh^{-1}(\tan\frac{\theta}{2}) & \text{if } -\frac{\pi}{2} < \theta < \frac{\pi}{2} \\ -4\tanh^{-1}(\cot\frac{\theta}{2}) & \text{if } \frac{\pi}{2} < |\theta| < \pi \end{cases} \tag{B.3}$$

$$\int_0^{\pi} \frac{d\alpha}{\sin(\alpha+\theta)} = 2\log\left(\cot\frac{|\theta|}{2}\right), \tag{B.4}$$

in the form

$$\begin{aligned}
\tau^1_{1\,\text{static}} &= \frac{\sin\phi}{2\pi^2(1+k)r}\left\{-4(1-k)\frac{|\cos\theta|}{\gamma_1\gamma_2\sin\theta}\tanh^{-1}\left(\begin{cases}\tan\frac{\theta}{2} & \text{if } -\frac{\pi}{2}<\theta<\frac{\pi}{2}\\ \cot\frac{\theta}{2} & \text{if } \frac{\pi}{2}<|\theta|<\pi\end{cases}\right)\right.\\
&\quad + (1-k)\int_0^{\pi}\left[\frac{\tan(\alpha+\theta)\tan\alpha}{\Lambda(\alpha+\theta)} + \frac{\cot\theta}{\cos\alpha\Lambda(\pi/2+\theta)} - \frac{|\cos\theta|}{\gamma_1\gamma_2\cos(\alpha+\theta)\sin\theta}\right]d\alpha\\
&\quad \left.-(2-k-\chi)\int_0^{\pi}\left[\frac{\sin(\alpha+\theta)\cos(\alpha+\theta)\tan\alpha}{\Lambda(\alpha+\theta)} + \frac{\cos\theta\sin\theta}{\cos\alpha\Lambda(\pi/2+\theta)}\right]d\alpha\right\},\\
\tau^2_{2\,\text{static}} &= -\frac{\sin\phi}{2\pi^2 r}\left\{2\frac{\sin|\theta|}{\cos\theta}\log\left(\cot\frac{|\theta|}{2}\right) + \int_0^{\pi}\left[\frac{\cot(\alpha+\theta)\tan\alpha}{\Lambda(\alpha+\theta)} + \frac{\tan\theta}{\cos\alpha\Lambda(\pi/2+\theta)} - \frac{|\sin\theta|}{\cos\theta\sin(\alpha+\theta)}\right]d\alpha\right.\\
&\quad \left.-\frac{2+k-\chi}{1+k}\int_0^{\pi}\left[\frac{\sin(\alpha+\theta)\cos(\alpha+\theta)\tan\alpha}{\Lambda(\alpha+\theta)} + \frac{\cos\theta\sin\theta}{\cos\alpha\Lambda(\pi/2+\theta)}\right]d\alpha\right\},\\
\tau^1_{2\,\text{static}} &= \frac{\cos\phi}{2\pi(1+k)r}\left(\frac{1-\chi}{\gamma_1\sqrt{-\gamma_2}+\gamma_2\sqrt{-\gamma_1}} + \frac{1+k}{\sqrt{-\gamma_2}+\sqrt{-\gamma_1}}\right)\\
&\quad -\frac{\sin\phi}{2\pi^2(1+k)r}\int_0^{\pi}\left\{\frac{\tan\alpha}{\Lambda(\alpha+\theta)}\left[(1-\chi)\sin^2(\alpha+\theta) - (1+k)\cos^2(\alpha+\theta)\right]\right.\\
&\quad \left.-\frac{1}{\Lambda(\pi/2+\theta)\cos\alpha}\left[(1-\chi)\cos^2\theta - (1+k)\sin^2\theta\right]\right\}d\alpha,\\
\tau^2_{1\,\text{static}} &= \frac{\cos\phi}{2\pi(1+k)r}\left(\frac{1-\chi}{\sqrt{-\gamma_2}+\sqrt{-\gamma_1}} + \frac{1-k}{\gamma_1\sqrt{-\gamma_2}+\gamma_2\sqrt{-\gamma_1}}\right)\\
&\quad +\frac{\sin\phi}{2\pi^2(1+k)r}\int_0^{\pi}\left\{\frac{\tan\alpha}{\Lambda(\alpha+\theta)}\left[(1-\chi)\cos^2(\alpha+\theta) - (1-k)\sin^2(\alpha+\theta)\right]\right.\\
&\quad \left.-\frac{1}{\Lambda(\pi/2+\theta)\cos\alpha}\left[(1-\chi)\sin^2\theta - (1-k)\cos^2\theta\right]\right\}d\alpha.
\end{aligned} \tag{B.5}$$

The limits when θ equals 0 or π in Eq. (B.5)$_1$ and when θ equals $\pi/2$ or $3\pi/2$ in Eq. (B.5)$_2$ are

$$\begin{aligned}
\tau^1_{1\,\text{static}} &= \frac{\sin\phi}{2\pi^2(1+k)r}\left\{-\frac{2}{\gamma_1\gamma_2} + (1-k)\int_0^{\pi}\left[\frac{\tan^2\alpha}{\Lambda(\alpha)} - \frac{\sin\alpha}{\gamma_1\gamma_2\cos^2\alpha}\right]d\alpha\right.\\
&\quad \left.-(2-k-\chi)\int_0^{\pi}\frac{\sin^2\alpha}{\Lambda(\alpha)}d\alpha\right\}, \quad \text{for } \theta = 0, \pi,
\end{aligned} \tag{B.6}$$

$$\begin{aligned}
\tau^2_{2\,\text{static}} &= \frac{\sin\phi}{2\pi^2 r}\left\{-2 + \int_0^{\pi}\left[\frac{\tan^2\alpha}{\Lambda(\alpha+\pi/2)} - \frac{\sin\alpha}{\cos^2\alpha}\right]d\alpha\right.\\
&\quad \left.-\frac{2+k-\chi}{1+k}\int_0^{\pi}\frac{\sin^2\alpha}{\Lambda(\alpha)}d\alpha\right\}, \quad \text{for } \theta = \pi/2, 3\pi/2.
\end{aligned} \tag{B.7}$$

Appendix C. Green's function for tractions on a line element inclined at $\theta + \phi$ for linear isotropic (compressible) elasticity and quasi-static deformation

For linear, isotropic and compressible elasticity, the quasi-static Green's function is [10]:

$$
\begin{aligned}
u_1^1 &= \frac{1}{8\pi\mu(1-v)}[-(3-4v)\log r + \cos^2\theta],\\
u_2^2 &= \frac{1}{8\pi\mu(1-v)}[-(3-4v)\log r + \sin^2\theta],\\
u_2^1 &= u_1^2 = \frac{\sin\theta\cos\theta}{8\pi\mu(1-v)},
\end{aligned}
\tag{C.1}
$$

where v is Poisson's ratio and μ the shear modulus.

Taking the gradient of Eqs. (C.1) and employing the elastic constitutive tensor, the components of the Green's functions for applied tractions on a plane inclined at $\theta + \phi$ are

$$
\begin{aligned}
\tau_1^1 &= -\sin\phi \frac{1-2v+2\cos^2\theta}{4\pi(1-v)r},\\
\tau_2^2 &= -\sin\phi \frac{1-2v+2\sin^2\theta}{4\pi(1-v)r},\\
\tau_2^1 &= -\frac{(1-2v)\cos\phi + 2\sin\phi\cos\theta\sin\theta}{4\pi(1-v)r},\\
\tau_1^2 &= \frac{(1-2v)\cos\phi - 2\sin\phi\cos\theta\sin\theta}{4\pi(1-v)r}.
\end{aligned}
\tag{C.2}
$$

The case of an incompressible material can be obtained from Eqs. (C.2) simply by setting $v = 1/2$. It may be important to note that for $\phi = 0$ and $\phi = \pi$ all components of the Green's function for tractions vanish in the incompressible case. Moreover, $\tau_2^1 = \tau_1^2$ in the incompressible case or when $\phi = \pi/2$ or $\phi = 3\pi/2$.

References

[1] M.P. Ariza, J. Dominguez, Dynamic BE analysis of 3-D cracks in transversely isotropic solids, Comput. Methods Appl. Mech. Engrg. 193 (2004) 765–779.
[2] J. Balas, J. Sladek, V. Sladek, Stress Analysis by Boundary Element Methods, Elsevier, Amsterdam, 1989.
[3] D.E. Beskos, Boundary element methods in dynamic analysis: Part II (1986–1996), Appl. Mech. Rev. 50 (1997) 149–197.
[4] C. Besnainou, From wood mechanical measurements to composite material for musical instruments - new technology for instrument makers, Mrs Bull 20 (3) (1995) 34–36.
[5] D. Bigoni, D. Capuani, Green's function for incremental nonlinear elasticity: shear bands and boundary integral formulation, J. Mech. Phys. Solids 50 (2002) 471–500.
[6] D. Bigoni, D. Capuani, Time-harmonic Green's function and boundary integral formulation for incremental nonlinear elasticity: dynamic of wave patterns and shear bands, J. Mech. Phys. Solids 53 (2005) 1163–1187.
[7] D. Bigoni, M. Gei, G. Franceschini, Thermoelastic small-amplitude wave propagation in nonlinear elastic multilayers, Math. Mech. Solids 9 (2004) 555–568 (special issue dedicated to Prof. R.W. Ogden).
[8] M.A. Biot, Mechanics of incremental deformations, J. Wiley and Sons, New York, 1965.
[9] G. Bissinger, Modern vibration measurement techniques for bowed string instruments – testing of acoustic stringed musical instruments, Exp. Techniques 25 (4) (2001) 43–46.
[10] M. Bonnet, Boundary Integral Equation Methods for Solids and Fluids, Wiley & Sons, New York, 1995.
[11] M. Brun, D. Capuani, D. Bigoni, A boundary element technique for incremental, nonlinear elasticity. Part I: Formulation, Comput. Methods Appl. Mech. Engrg. 192 (2003) 2461–2479.
[12] M. Brun, D. Capuani, D. Bigoni, A boundary element technique for incremental, nonlinear elasticity. Part II: Bifurcation and shear bands, Comput. Methods Appl. Mech. Engrg. 192 (2003) 2481–2499.
[13] E.J. Brunelle, S.R. Robertson, Vibrations of an initially stressed thick plate, J. Sound Vibr. 45 (1976) 405–416.
[14] T.A. Cruse, Boundary Element Analysis in Computational Fracture Mechanics, Kluver, Dordrecht, 1988.
[15] T.A. Cruse, F.J. Rizzo, A direct formulation and numerical solution of the general transient elastodynamic problem I, J. Math. Anal. Appl. 22 (1968) 244–259.
[16] M. Denda, C.Y. Wang, Y.K. Yong, 2-D time-harmonic BEM for solids of general anisotropy with application to eigenvalue problems, J. Sound Vibr. 261 (2003) 247–276.
[17] J. Dominguez, Boundary Elements in Dynamics, Computational Mechanics Publications co-published with Elsevier Applied Science, 1993.
[18] M.A. Dowaikh, R.W. Ogden, On surface waves and deformations in a pre-stressed incompressible elastic solids, IMA J. Appl. Math. 44 (1990) 261–284.
[19] M.A. Dowaikh, R.W. Ogden, Interfacial waves and deformations in pre-stressed elastic media, Proc. R. Soc. Lond. A 443 (1991) 313–328.
[20] E. Drescher-Krasicka, J.R. Willis, Mapping stress with ultrasound, Nature 384 (1996) 52–55.
[21] L. Gaul, M. Kögl, M. Wagner, Boundary Element Methods for Engineers and Scientists. An Introductory Course with Advanced Topics, Springer, 2003.
[22] K.F. Graff, Wave Motion in Elastic Solids, OSU Press, 1991.
[23] G. Herrmann, A.E. Armenakas, Vibrations and stability of plates under initial stress, J. Mech. Division ASCE 86 (1960) 458–487.
[24] S. Hirose, M. Kitahara, Elastic wave scattering by inhomogeneous and anisotropic bodies in a half space, Earthquake Engrg. Struct. Dyn. 18 (1989) 285–297.

[25] A.K. Jha, D.J. Inman, Importance of geometric non-linearity and follower pressure load in the dynamic analysis of a gossamer structure, J. Sound Vibr. 278 (2004) 207–231.
[26] N. Kame, J.R. Rice, R. Dmowska, Effects of pre-stress state and rupture velocity on dynamic fault branching, J. Geophys. Res. 108 (2003) 1–19.
[27] L. Kari, On the dynamic stiffness of preloaded vibration isolators in the audible frequency range: Modeling and experiments, J. Acous. Soc. Am. 113 (2003) 1909–1921.
[28] F. Kausel, J.M. Roësset, Semianalytic hyperelement for layered strata, J. Engrg. Mech. Div. ASCE 103 (EM4) (1977) 569–589.
[29] J.T. Kim, C.B. Yun, Y.S. Ryu, H.M. Cho, Identification of prestress-loss in PSC beams using modal information, Struct. Engrg. Mech. 17 (2004) 467–482.
[30] M. Kogl, L. Gaul, A 3-D boundary element method for dynamic analysis of anisotropic elastic solids, CMES-Comput. Modelling Engrg. Sciences 1 (2000) 27–43.
[31] J.C. Lachat, J.O. Watson, Effective numerical treatment of boundary integral equations: a formulation for elastostatics, Int. J. Numer. Methods Engrg. 10 (1976) 991–1005.
[32] G.D. Manolis, D.E. Beskos, Boundary Element Methods in Elastodynamics, Unwin Hyman Ltd, London, 1988.
[33] V. Mantic, A new formula for the C-matrix in the Somigliana identity, J. Elasticity 33 (1993) 191–201.
[34] V. Mantic, F. Paris, Integral kernels in the 2D Somigliana displacement and stress identities for anisotropic materials, Computational Mechanics 22 (1998) 77–87.
[35] F. Medina, J. Penzien, Infinite elements for elastodynamics, Earthquake Engrg. Struct. Dyn. 10 (1982) 699–709.
[36] K.D. Murphy, L.N. Virgin, S.A. Rizzi, The effect of thermal prestress on the free vibration characteristics of clamped plates: theory and experiment, J. Vibrat. Acoust. ASME 119 (1997) 243–249.
[37] D. Nardini, C.A. Brebbia, A new approach to free vibration analysis using boundary elements, in: C.A. Brebbia (Ed.), Boundary Element Methods in Engineering, Springer, Berlin, 1982, pp. 312–326.
[38] R.W. Ogden, D.A. Sotiropulos, On interfacial waves in pre-stressed layered incompressible elastic solid, Proc. Roy. Soc. Lond. A 450 (1995) 319–341.
[39] O. Paul, H. Baltes, Mechanical behavior and sound generation efficiency of prestressed, elastically clamped and thermomechanically driven thin film, J. Micromech. Microengrg. 9 (1999) 19–29.
[40] D. Polyzos, S.V. Tsinopoulos, D.E. Beskos, Static and dynamic element analysis in incompressible linear elasticity, Eur. J. Mech., A/Solids 17 (1998) 515–536.
[41] J. Przybylski, L. Tomski, M. Golebiowska-Rozanow, Free vibration of an axially loaded prestressed planar frame, J. Sound Vibr. 189 (1996) 609–624.
[42] E. Radi, D. Bigoni, D. Capuani, Effects of pre-stress on crack-tip fields in elastic, incompressible solids, Int. J. Solids Structures 39 (2002) 3971–3996.
[43] D.G. Roxburgh, R.W. Ogden, Stability and vibration of pre-stressed compressible elastic plates, Int. J. Engrg. Sci. 32 (1994) 427–454.
[44] E.I. Ryzhak, On stable deformation of "unstable materials in a rigid triaxial testing machine, J. Mech. Phys. Solids 41 (1993) 1345–1356.
[45] E.I. Ryzhak, On stability of homogeneous elastic bodies under boundary-conditions weaker than displacement conditions, Quart. J. Mech. Appl. Math. 47 (1994) 663–672.
[46] M. Sjöberg, L. Kari, Nonlinear isolator dynamics at finite deformations: an effective hyperelastic, fractional derivative, generalized friction model, Nonlinear Dynamics 33 (2003) 323–336.
[47] C. Sultan, R. Skelton, A force and torque tensegrity sensor, Sensors Actuators A-Physical 112 (2004) 220–231.
[48] M. Tanaka, V. Sladek, J. Sladek, Regularization techniques applied to boundary element methods, ASME Appl. Mech. Rev. 47 (1994) 457–499.
[49] S.M. Vogel, F.J. Rizzo, An integral equation formulation of three dimensional anisotropic elastostatic boundary value problems, J. Elasticity 3, 1–14.
[50] W. White, S. Valliappan, I.K. Lee, Unified boundary for finite dynamics models, J. Engrg. Mech. Div. ASCE 103 (1977) 949–964.
[51] C. Zhao, T. Liu, Non-reflecting artificial boundaries for modelling scalar wave propagation problems in two-dimensional half space, Comput. Meth. Appl. Mech. Engrg. 191 (2002) 4569–4585.